

A study of simulated histories of reionization with merger trees of HII regions

Jonathan Chardin*, Dominique Aubert, and Pierre Ocvirk

Observatoire Astronomique de Strasbourg, Université de Strasbourg, CNRS UMR 7550, 11 rue de l'Université, F-67000 Strasbourg, France

Accepted / Received

ABSTRACT

Aims. We describe a new methodology to analyze the reionization process in numerical simulations: the chronology and the geometry of reionization is investigated by means of merger histories of individual HII regions.

Methods. From the merger tree of ionized patches, one can track the individual evolution of the regions properties such as e.g. their size, or the intensity of the percolation process by looking at the formation rate, the frequency of mergers and the number of individual HII regions involved in the mergers. We apply the merger tree technique to simulations of reionization with three different kinds of ionizing source models and two resolutions. Two of them use star particles as ionizing sources. In this case we confront two emissivity evolutions for the sources in order to reach the reionization at $z \sim 6$. As an alternative we built a semi-analytical model where the dark matter halos extracted from the density fields are assumed as ionizing sources.

Results. We then show how this methodology is a good candidate to quantify the impact of the adopted star formation on the history of the observed reionization. The semi-analytical model shows a homogeneous reionization history with 'local' hierarchical growth steps for individual HII regions. On the other hand auto-consistent models for star formation tend to present fewer regions with a dominant region in size which governs the fusion process early in the reionization at the expense of the 'local' reionizations. The differences are attenuated when the resolution of the simulation is increased.

Key words. Reionization, HII regions , first stars - Methods: numerical

1. Introduction

The first generation of stars appears after the period of dark ages (between $z \sim 1090$ and $z \sim 20$), creating a multitude of distinct HII regions in the Universe. These regions eventually merge with other ionized regions, leading to a total reionization of the Universe. The diffusion of CMB photons on the electrons released during reionization (see e.g. Komatsu et al. 2009) and the absorption features in the spectra of high redshift quasars (see e.g. Fan et al. 2006, Willott et al. 2007) suggest that the end of reionization occurred at $z \sim 11 - 6$, with an average neutral fraction of hydrogen between 10^{-4} and 10^{-6} (see Fan et al. 2006).

Many models (see e. g. Barkana & Loeb 2004, Furlanetto et al. 2004b, Zahn et al. 2007, Mesinger & Furlanetto 2007, Choudhury et al. 2009) and simulation techniques (Abel et al. 1999, Gnedin & Abel 2001, Razoumov et al. 2002, Iliev et al. 2006a, Trac & Cen 2007, Aubert & Teyssier 2008, Finlator et al. 2009a and Petkova & Springel 2009) have been proposed to investigate the impact of the radiative transfer on the reionization epoch. See Trac & Gnedin (2009) for a complete review of these models. In parallel, semi-analytic models were developed (Barkana & Loeb (2004), Furlanetto et al. (2004b), Zahn et al. (2007), Mesinger & Furlanetto (2007), Choudhury et al. (2009)), mostly based on the 'excursion set formalism' method (Bond et al. (1991)) where both the source

distribution and ionization fields are derived from the density fields.

In this context, one challenge is to describe the geometry and the time sequence of the reionization as they will be influenced by e.g. the formation rate of ionizing sources, the distribution of their formation sites or the size and growth of HII regions. Aiming at this description, many theoretical studies have thus been conducted focusing on the global evolution of physical fields such as the ionized fraction or temperature (see e.g. Aubert & Teyssier 2010, Finlator et al. 2009b). Alternately, many groups have undertaken analyzes to characterize this period but by focusing on the properties of individual HII regions (Iliev et al. 2006b, Zahn et al. 2007, McQuinn et al. 2007, Lee et al. 2008, Croft & Altay 2008, Shin et al. 2008, Friedrich et al. 2011).

With the current article, we also aim at investigating the chronology and geometry of the reionization through numerical simulations. In particular, we describe the process through the study of *the merger process* of HII regions and for this purpose we track the individual histories of the ionized regions formed in numerical simulations. Using this point-of-view, we combine the analysis in terms of individual HII regions with the temporal evolution of global fields. As a consequence, it results in a 'local' perspective with *a set of histories of reionization*, allowing to study their scatter throughout a cosmological volume. This will be an alternative approach to those already undertaken.

* e-mail: jonathan.chardin@astro.unistra.fr

In this paper, we first focus on the procedure to separate the different HII regions and to track each of them along time. For this purpose, we follow many other investigations (Iliev et al. 2006b, Shin et al. 2008 and Friedrich et al. 2011) by using a *Friends-of-friends algorithm* (FOF) to characterize the different ionized regions. Then, to follow the HII regions' properties with time or redshift, we build their *merger tree*. Using the merger tree and investigating its properties to infer the redshift evolution of the HII regions' formation number, their size evolution and their merger history, we suggest a new way to constrain the evolution of the reionization process.

We test the method on three models for the ionizing sources in order to quantify their impact on the simulated reionization history. We also quantify the impact of the spatial resolution of the simulations on the history by performing simulations with sizes of 200 and 50 Mpc/h boxes. By comparing the resulting reionization histories, we show how different source prescriptions lead to different properties on the evolution of HII regions as reionization progresses.

This paper is organized as follows. In Section 2, we present the tools developed to investigate the history of the reionization in simulations such as the FOF algorithm and the merger tree of HII regions. In Section 3, we detail the properties of the simulations that we study. In Section 4, first, we present our results in terms of general quantities such as the ionization fraction or the optical depth evolution. Then, in section 5, we compare the different histories of each model enlightened with the merger tree methodology. We finally discuss these results and their limits in section 6 and get our conclusions.

2. Analysing merger trees of HII regions

2.1. Rationale

Merger trees have been used for 20 years in e.g. the theoretical studies of galaxy formation (see e.g. Lacey & Cole (1993) and Kauffmann & White (1993)). More recently seminal works such as Furlanetto et al. (2004a) and subsequent analytical and semi-analytical investigations have used excursion set formalisms to construct histories of HII regions during reionization. Even though it is strongly connected to the aforementioned works, the current paper aims at using merger trees differently. The trees *are extracted from simulations*, are used and *analyzed as objects worthy of studies for their own properties*: in other words we analyze the simulated HII region merger histories from the merger tree they produce. The latter is not an intermediate to provide higher levels prediction such as e.g. statistics on 21cm signal, but is itself a probe of the properties of the simulation. On a broader perspective, the methodology presented here could be compared to genus or skeleton calculations as a reproductive and quantitative mean to discuss the simulated process. It is thus complementary to power spectra or time-evolution of average quantities for instance. In practice, in addition to tracking individual HII regions, we are thus led to analyze the "graph" properties of tree-based data as shown hereafter and draw conclusions on the simulated physics. Hereafter, we present briefly our implementation of the classic FOF technique to identify HII regions and the procedure to build merger trees. Additional details of these classic tools can be found in the appendix.

2.2. FOF identification of HII regions

We have developed a FOF algorithm which is able to separate the different HII regions at a given instant in snapshots of simulations and allocate them an identification number. The following description of this *Friends-of-friends method* is similar to that used in previous studies (Iliev et al. 2006b, Shin et al. 2008, Friedrich et al. 2011). The ionization state of the gas is sampled on a regular grid.

First we define the status of the box cells in terms of ionization fraction. The rule we have adopted is that a cell is ionized if it has an ionization fraction $x \geq 0.5$ (as often used in other works e.g. Iliev et al. 2006b, Shin et al. 2008, Friedrich et al. 2011). An individual HII region is defined by an identification number (ID hereafter). Then if a cell is ionized and has an ID, then all its ionized nearest neighbors belong to the same ionized region and thus share the same ID. Our definition of nearest neighbors is limited to 6 cells along the main directions. One single isolated cell is then considered as a single ionized region. More details about the FOF implementation can be found in appendix A.

We have to note that the FOF procedure is not without caveats. Thereby we could have adopted greater values for the ionization fraction threshold for example. We can then imagine that HII regions would be more divided and more numerous with smaller sizes in this case, possibly leading to different reionization histories. In appendix, we show that the statistics of the regions depend weakly on this specific value of the ionization threshold in the 0.3-0.9 range, except for the smallest regions with recombining episodes. The FOF technique can also connect distant regions with ionized bridges, an effect that might be undesirable. Alternately we could have chosen other methods for the identification such as the *spherical average* method described by Zahn et al. (2007). In this case the distribution of HII region sizes would have been smoother (see Friedrich et al. 2011). We have chosen the FOF method because it allows to follow regions from snapshot to snapshot in order to build the merger tree, which is a feature that the *spherical average* method does not allow. We thus have to keep in mind the features of the method when we will give our conclusion in the next.

2.3. Merger tree

The identification of the ionized regions in each snapshot of a simulation being known, the merger tree of HII regions can be built. Such a tree aims at tracking the identification number of an ionized region in order to follow the evolution of its properties along time (see appendix B for details in the merger tree implementation).

In Figure 1 an example of a merger tree is represented where each black line represents an ID evolution for a distinct HII region. As reionization progresses, there is a growing number of ionized regions to follow, as represented by the growing number of branches in the tree. We can also follow the merger process between HII regions when several branches of the tree lead to the same ID. We observe a decrease in the number of regions until there remains a single one at the end of reionization.

From the merger tree thus constructed, we will be able to follow the properties of ionized regions during the entire simulated reionization. Indeed, it will be possible to study the temporal evolution of each HII region, their individual

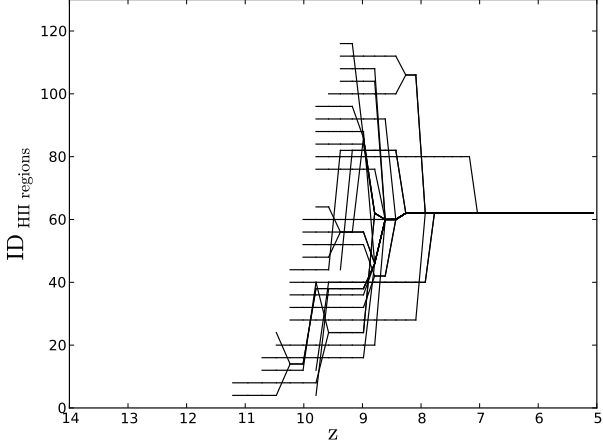


Fig. 1. Illustration of the merger tree of HII regions. Each black line represents an ID evolution with the redshift for a distinct HII region. For clarity, we represent here only the ID evolution for 30 regions. Mergers occur when several branches of the tree lead to the same ID.

merging history, their geometric properties and enlighten in a different way the scenario of reionization.

Let us note that this technique can be sensitive to the snapshot sampling of the simulations. Non-regularly spaced snapshots or a sparse sampling can weaken the conclusions obtained with a merger tree. Preliminary experiments, by taking e.g. half of the snapshots, have shown that our results seem to be robust, however the quantitative conclusions may be prone to variations.

In figure 2 we illustrate the typical properties that can be investigated through the merger tree :

- the number of new HII regions between two snapshots.
- the number of growing ionized regions.
- the number of HII regions which recombine.
- the number of HII regions resulting from mergers.
- the number of parents involved for a HII region resulting from mergers

3. Simulations

3.1. Gas Dynamics and Post-processed Radiative transfer

In this section we aim at describing the cosmological simulations of reionization performed and analyzed with the merger tree methodology. These simulations were part of a set of experiments at several resolutions and fully described in Aubert & Teyssier (2010) and only a brief summary of the methodology will be given here.

The evolution of the gas and sources distribution were provided by outputs of the RAMSES cosmological code (Teyssier 2002) that handles the co-evolution of dark matter, gas and star particles using an adaptive mesh refinement strategy. The hydrodynamical equations are solved thanks to a second order Godunov Scheme with an HLLC Riemann Solver. The gas is assumed to be perfect with a 5/3 polytropic index. Metals are included and taken in account in the cooling of the gas. The star formation is included following the prescription of Rasera & Teyssier (2006) as well as supernovae feedback.

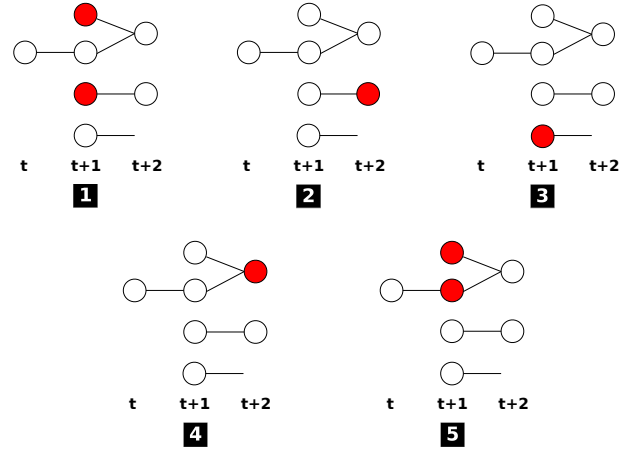


Fig. 2. Illustration of the properties that we can follow with the merger tree. In each diagram, red items symbolise the kind of properties that we follow. 1: the number of new HII regions between two snapshots, 2: the number of growing ionized regions, 3: the number of HII regions which recombine, 4: the number of HII regions resulting from mergers and 5: the number of parents involved for an HII region resulting from mergers

Initial conditions were generated on 1024^3 grids, according to the WMAP 5 cosmology (Komatsu et al. (2009)) using the MPgatic package and white noise statistics from the Horizon collaboration (Prunet et al. (2008)). Two box sizes were considered, 50 and 200 Mpc/h, both with a 1024^3 coarse grid resolution+ 3 levels of refinement and simulations were conducted down to $z \sim 5.5$. The refinement strategy is quasi-lagrangian with finer levels being triggered when the mass within a cell is 8 times the mass resolution. The large box is less subject to finite-volume variance effects but lacks resolution whereas the 50 Mpc/h box better resolve small scales physics (such as star formation) but is more prone to cosmic variance and its percolation process during reionization may be already affected by periodic boundary conditions

The radiative transfer was included as a post-processing step using the ATON code (Aubert & Teyssier 2008) in all simulations. It tracks the propagation of radiation on a 1024^3 coarse grid using a moment-based description of the radiative transfer equation. It can reconcile the high resolution and the intensive time-stepping of the calculation thanks to Graphics Processing Units (GPUs) acceleration obtained through NVidia's CUDA extension to C (see Aubert & Teyssier (2010) for further details of the implementation). ATON also tracks atomic hydrogen processes such as heating/cooling and photo-ionization and can handle multiple group of frequencies, even though in the current work only a single group of photon has been dealt with. The typical photon energy is 20.26 eV, corresponding to the average energy of an hydrogen ionizing photon emitted by a 50 000 K black body: such spectrum is a good approximation of a salpeter IMF integrated over the stellar particles mass assumed here (see e.g. Baek et al. (2009)). Calculations were run on 64-128 M2068 NVidia GPUs on the hybrid sections of the Titane and Curie supercomputers hosted by the CCRT/CEA facilities. Having post-processed the simulations, we applied the merger tree methodology

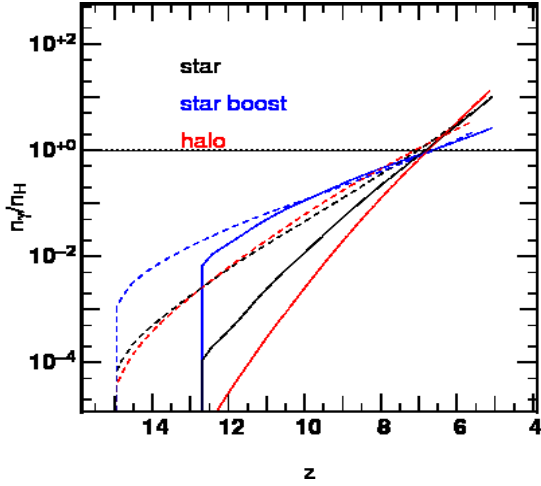


Fig. 3. Redshift evolution of the cumulative number of ionizing photons emitted by the sources relative to the number of hydrogen atoms. The horizontal line stand for one photon per atom. Solid (resp. dashed) lines stand for the 200 (resp. 50) Mpc/h simulations. Black, blue and red curve stand respectively for the ‘Star’, ‘Boosted Star’ and ‘Halo’ models of ionizing sources.

described in the previous section to the ionisation fraction field degraded at a 512^3 resolution, making them easier to analyse.

3.2. Ionising source models

At each resolution, three different models were considered for the sources: two considered the self-consistent stellar particles spawned by the cosmological simulation code. The third one uses dark matter halos as proxies for the sources. All the models were tuned by trial and error to provide a complete reionization by $z \sim 6.5 - 5.5$ and a half-reionization at $z \sim 7$. Sources were included in the radiative transfer calculation following the same procedure as in Aubert & Teyssier (2010).

3.2.1. ‘Star’ models

The star formation recipe is described in Rasera & Teyssier (2006) and assumes that above a given baryon over-density ($\delta \sim 5$ in our case), gas transforms into constant mass stars ($1 \times 10^6 M_\odot$ and $2 \times 10^4 M_\odot$ in 200/50 Mpc/h boxes) with a given efficiency ($\epsilon = 0.01$).

The number of stellar particles found at $z \sim 8.5$ (that corresponds to the peak of HII regions number as seen hereafter) is 8500 (resp. 35 500) in the 200 Mpc/h (resp. 50 Mpc/h) simulations. Even though it is now standard, the modelisation of the formation of ‘stellar’ particles in cosmological simulations remains a complex and subtle matter. Among other effects, it depends strongly on the resolution: the growth of non-linearities is scale-dependent and as a consequence the simulated star formation rate depends on the ability of the simulation to resolve high-density peaks (see e.g. Springel & Hernquist (2003), Rasera & Teyssier (2006) and references therein). Therefore poorly resolved simulations tend to develop a population of stars at later times and at a slower rate than more resolved ones.

This limitation is further emphasized during the reionization epoch at large z . As a direct consequence the amount of ionizing photons is usually under-evaluated if taken directly from star particles even though the situation improves as the non-linearities evolves in the simulations. For instance, with the number of resolution elements and refinement strategy used in the current work, a 12.5 Mpc/h box would be necessary to achieve a convergence in the number of emitted photons (Aubert & Teyssier (2010)). Otherwise, the star particles may even be too scarce to reionize the cosmological box. Furthermore, these sources are subject to stochasticity: they contribute to the UV flux only during the lifetime of strong UV-emitting stars (that we chose to be 20 Myrs). As this component fade away in a given ‘stellar particle’, the latter may not be replaced by a neighbour. Until a stationary regime of source renewal is installed, these numerical artefacts due to source discreteness and lack of convergence may lead to ‘blinking’ emitters of numerical nature, and therefore to artificial recombining HII regions unsustained by inner sources, without any relation to actual starburst episodes.

On the other hand, these ‘stellar’ sources are directly generated from the simulation, are simulated self-consistently with the gas physics and do not require an additional processing to compute the sources locations and emissivities. One may suggest that a simple correction may be enough to correct from the low resolution effects. The simplest is to consider that stellar particles sample correctly the location of the main UV sources and a constant fudge factor would provide the adequate number of ionizing photons to reionize at $z \sim 7 - 6$. Such a model will be named as ‘SXX’ hereafter, where ‘XX’ stands for 200 or 50 depending on the box size. A more sophisticated one requires that not only the adequate number of photons is generated at $z = 6$ but also at each instant. Since the lack of resolution is more critical at early times, it implies a stronger correction at high z than later on. Aubert & Teyssier (2010) have shown that the correction is exponential with characteristic times depending on the resolution. A drawback of this type of correction is the fact that sources end up as being individually ‘decaying’ with time: if the renewal rate of stellar particles is not high enough, this decay could impact the simulated reionization. In this model, ‘stellar particles’ have *boosted* emissivities per baryon at early times and will be named ‘SBXX’ hereafter, XX standing for the box size. It should be noted that the density contrast chosen here to trigger star formation can be seen as low and is chosen to allow star formation at our moderate spatial resolution and at redshifts where non-linearities are weak at our scales. The value chosen here is similar to the one used by e.g. Nagamine et al. (2000) at the same resolution and is slightly more permissive than most of the thresholds reviewed e.g. in Kay et al. (2002) with typical values of $\delta \sim 10$. However, even with such criteria, significant factors should be applied to the luminosity of these stellar particles to produce enough photons to obtain ‘standard reionizations’ histories. As shown hereafter, the ionized ‘patchiness’ of these models tend to be less structured on small scales than halo-based models while nevertheless having their overlap process sharing the same global properties. Overall it indicates that star particles are not overproduced.

In Fig. 3, one can see that the S200 and S50 ‘stellar’ models show different slopes for the cumulative number of photons. It results from the fact that the same number of

photons must be produced from a smaller number of star particles and on a shorter period for the large box. At both resolutions, 2 ionizing photons per hydrogen atom have been produced when reionization is completed at $z \sim 6.5$. The SB models are as expected ‘converged’: as the photon production become stationary, the same number of photons is produced in both box sizes. Compared to the ‘Star models’ emissivities, the ‘Boosted’ ones are greater at early times then smaller for $z < 7.5$, to achieve the reionization at the same epoch. On a more general note, one can see that ‘stellar’ particles appear earlier at high resolution as expected.

Quantitatively, we followed the simple modelisation of Baek et al. (2009) to assign an emissivity of 90 000 photons per stellar baryons over the lifetime of a source. For S50 and S200 the enhancement factors to account for convergence issue are respectively 3.8 and 30, while the boost temporal evolution of the SB50 and SB200 is equal to $\max(1, a \exp(k/t))$ with $(a, k[\text{Myr}]) = (1.2, 1500)$ for SB50 and $(1.2, 3000)$ for SB200, t being the cosmic time.

3.2.2. Halo sources

As a second choice we adopt a semi-analytical model for the production of ionizing sources based on dark matter halos. Each halo is assumed as a star formation site with an emissivity proportional to the halo mass. This procedure is largely inspired by the work of Iliev et al. (2006b) where a constant mass-to-light ratio is assumed such as the ionizing flux of each halo has the following expression:

$$\dot{N}_\gamma = \alpha M \quad (1)$$

where α is the emissivity coefficient. Here we have chosen values of $\alpha = 5.9 \times 10^{43}$ and $\alpha = 3.5 \times 10^{42}$ photons/s/ M_\odot for both 200 and 50 Mpc/h boxes respectively. These values were chosen in order to reach a reionization at $z \sim 6.5 - 6$ similar to the ‘Star’ and ‘Boosted Star’ models. Halos were detected using the parallel FoF finder of Courtin et al. (2011), with a linking length of $b=0.2$ and a minimal mass of 10 particles. This minimal mass corresponds to $9.8 \times 10^7 M_\odot$ for the 50 Mpc/h box and $6.3 \times 10^9 M_\odot$ for the 200 Mpc/h box, implying that all halos can be considered as emitters. The number of halos found at $z \sim 8.5$ is 33 100 (resp. 285 000) in the 200 Mpc/h (resp. 50 Mpc/h) simulations. It should also be emphasized that, contrary to ‘Star’ and ‘Boosted Star’ models, a whole spectrum of mass, and thus emissivities, is available for halos. No lifetime has been assigned to these sources and a halo would produce photons as soon as it is being detected until it disappears or merge. In the following sections we will refer to this semi-analytical star formation simulations with the following acronyms: “H200” or “H50” for both box sizes of 200 and 50 Mpc/h.

In Fig. 3, one can see that ‘Halo 50’ follows closely ‘Star 50’, implying that provided the appropriate correction, stars can mimic halos emission history. A greater difference can be seen in the 200 Mpc/h box, where the ‘Halo 200’ model shows a greater slope than the ‘Star 200’ model: there exists a greater difference in the buildup of halos compared to the star population at lower resolution, due mostly to the difficulty to achieve star formation density thresholds in large scale simulations. At $z \sim 6.5$, roughly two photons per hydrogen atom were produced in all cases.

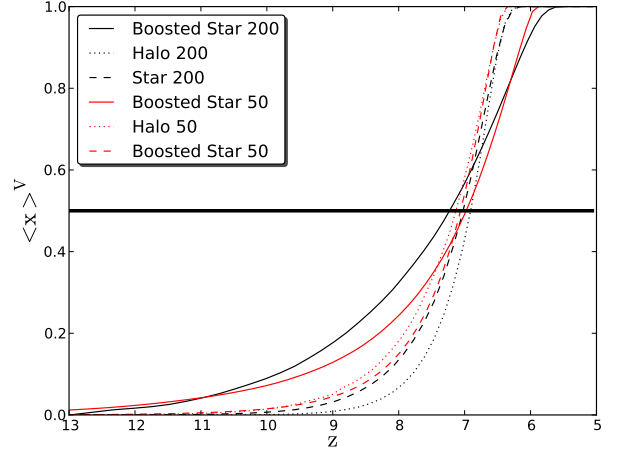


Fig. 4. Evolution of the volume weighted average ionization fraction with redshift for the six simulations.

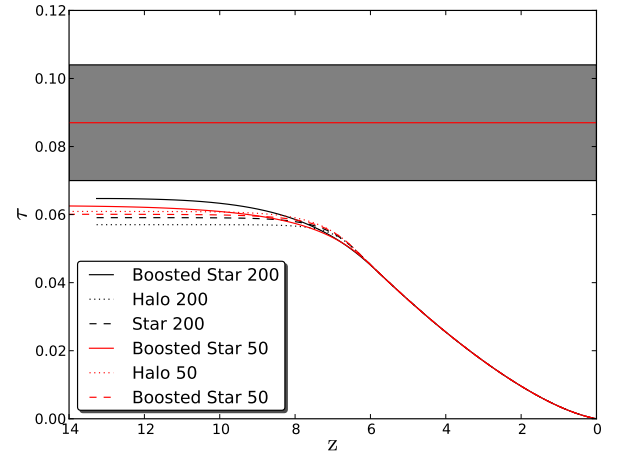


Fig. 5. Evolution of the Thomson optical depth with redshift for the six simulations.

4. Global features

4.1. Ionisation fraction

Figure 4 shows the evolution of the volume weighted average ionization fraction as a function of redshift for the three models and for both 200 and 50 Mpc/h boxes. Average ionization curves show a similar value of $\langle x \rangle \sim 0.5$ at a redshift of $z \sim 7$. At first glance we see that every models are comparable in terms of ionization fraction. The boosted star model just shows an earlier “take off” in the ionization curve than in both others models for the two box sizes. Conversely in the Star and Halo models the ionization curves “take off” later ($z \sim 10 - 9$) but the reionization is achieved earlier than in the boosted Star model. These differences are attenuated in the 50 Mpc/h box where the ionization histories become very close from one model to another.

4.2. Optical depth

Figure 5 shows the evolution of the optical depth as a function of redshift for the six simulations given by

$$\tau(z) = c\sigma_t \int_z^0 n_e(z) \frac{dt}{dz} dz \quad (2)$$

where σ_t is the Thompson cross section of the electron and $n_e(z) = \langle x(z) \rangle n_H(z)$ is the density of electrons released by ionized hydrogen atoms at redshift z . We also represent the constraint range obtained from the five year release of CMB measurement made by the *WMAP* collaboration (Komatsu et al. (2009)) at the 1σ level.

We immediately see that all the simulations converge in terms of optical depth. The 200 Mpc/h box simulations reach a same value at $z \sim 8$. The only difference being that the optical depth is slightly greater in the boosted Star model before $z \sim 8$. This is naturally explained by the fact that the ionization history is more extended in this model as seen with the ionization curve in figure 4. In the 50 Mpc/h box, the curves become almost superimposed from $z \sim 10$. Again this comforts us in saying that all the simulations are comparable.

4.3. Ionisation fields

The maps of figures 6 and 7 show the ionization field maps for the three models for both 200 and 50 Mpc/h boxes. In each figure, colour encodes an individual HII region detected by the FOF procedure.

At $z \sim 10.5$ and $z \sim 8.4$, the basic features of the 3 type of reionization can be spotted: SB models exhibit a few regions with large radii, whereas H models have smaller and numerous individual regions. S models are intermediate with larger ionized patch than detected in the halo-based simulations but more individual regions than found in the SB models. As such it reflects the differences in source modeling where halos are more numerous than stellar particles and therefore share ionizing photons over a larger number of weaker sources. On the other hand, SB models produce large regions at the earliest redshifts because of the strong initial correction to the source emissivity and which favors large regions and potentially early overlaps.

At the end of the reionization at $z \sim 6.9$ and in all models, a single large HII region is detected by the FOF method that results from a connected network of multiple ionized regions. Nonetheless, the Halo model presents a greater resilience to percolation as it presents a map more structured with more individual HII regions.

When the spatial resolution is increased with the 50 Mpc/h box, the figure 7 shows the same tendencies as in the 200 Mpc/h box. The H50 map presents the most important number of regions with the smallest sizes until late phases of the reionization and the SB50 still presents the lowest number of regions with the largest sizes. S50 still represents an intermediate case. Overall and as expected by the greater spatial resolution, ability to capture the clustering and larger number of sources in a 50 Mpc/h box, these maps present a greater level of granularity and more individual regions than the 200 Mpc/h versions.

5. Merger tree properties

Our main interest is to investigate the impact of the ionizing source models on the reionization history. Typically, we will see what quantities are retained from one model to another and how these models imprint differences on the history observed.

5.1. Evolution of the number density of HII regions

The figure 8 shows the evolution of the number density of ionized regions as a function of redshift for the three models of ionizing sources and for both box sizes. We distinguish in addition the number of each type of HII regions: new regions, those resulting from mergers, those expanding without merging and those recombining are respectively shown in blue, green, red and yellow. We note that the distributions present the same general shape regardless of the source model. They all show their maximum number of regions at broadly the same redshift z_{peak} for both spatial resolution respectively at $z \sim 8$ and $z \sim 9$ for 200 Mpc/h and 50 Mpc/h. Before z_{peak} , HII regions appear and expand, populating the box with more and more regions. We can refer to this period as the "pre-overlap" period where the reionization is dominated by the expansion and the birth of new HII regions. Conversely after z_{peak} , HII regions begin to merge intensively and decrease in number during an "overlap period", that continues until the reionization is completed. Even though the shape of the distributions are similar, the absolute number of HII regions is much greater in the Halo model than in the two 'stellar ones' and with a greater discrepancy in the 50 Mpc/h box. This absolute number remains within the same order of magnitude between the Star and the boosted Star model for both boxes. This difference is not surprising and typically reflects the difference in the relative number of ionizing sources produced from one model to another. Indeed the number of dark matter halos assumed as ionizing sources in the semi analytical model is greater than the number of auto-consistent ionizing sources generated in both Star models : at $z=8.5$ there are ~ 4 (resp. 8) times more halos than stellar particles in the 200 Mpc/h (resp. 50 Mpc/h) and it corresponds to the factor measured in terms of detected HII regions. Finally, when splitting these distribution in different types of ionized regions (new, expanding, merging and recombining), they follow the overall pattern of increase and decline after z_{peak} with differences detailed in the next section 5.2. Let us only mention the case of new regions that also follow the same pattern even though at face value mergers only affect pre-existing ionized patches. It should be reminded that as reionization progresses the amount of neutral volume decreases, limiting the possibility of having new sources in a neutral area. Hence, new regions are also affected by the overlapping process, albeit indirectly.

5.2. Number and volume fraction of the different types of HII regions

To emphasize differences in the histories of the various kind of regions, Fig. 9 shows the evolution of their relative proportion (rather than their number density) in terms of number and Fig. 10 presents the volume fraction of the whole simulated boxes occupied by each type of HII region.

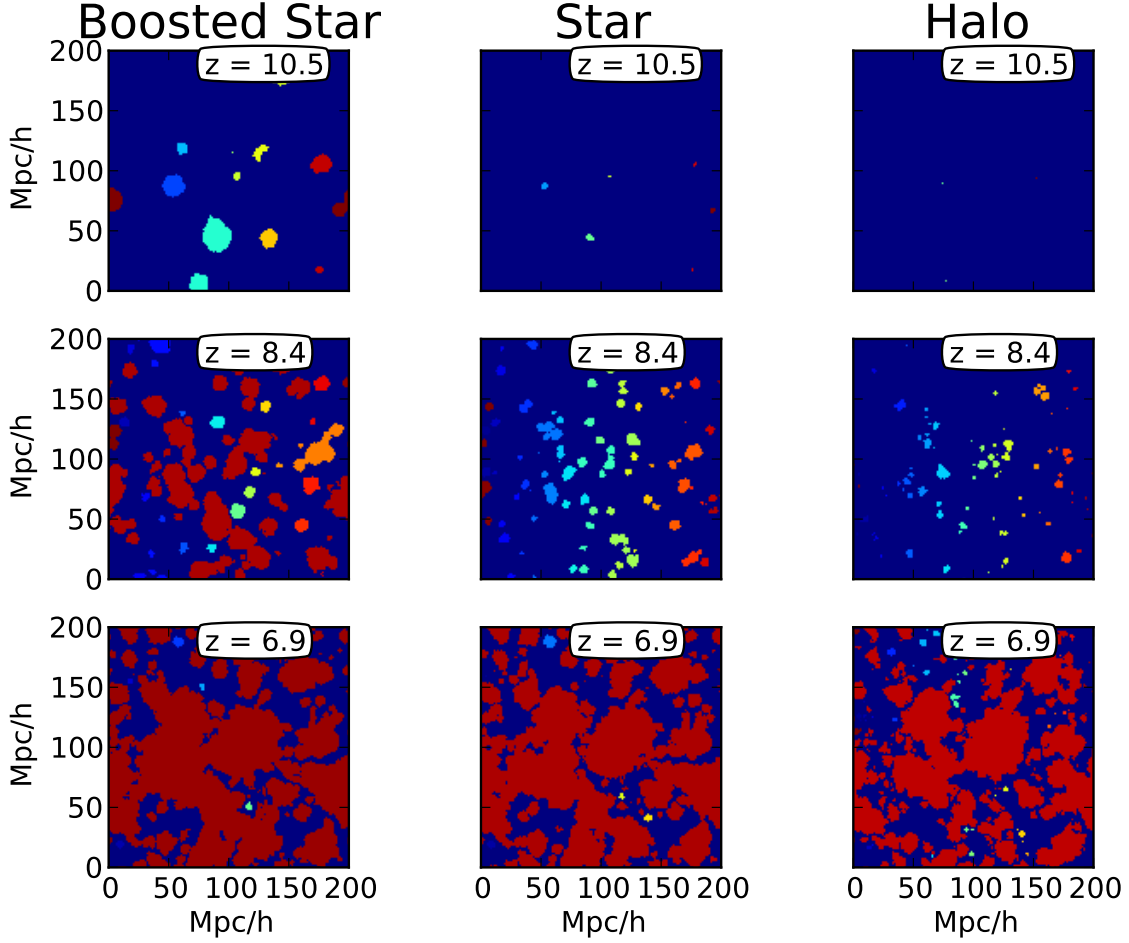


Fig. 6. Ionisation map for the three ionizing sources models for three distinct redshift for the 200 Mpc/h size box. The colours encode the different identification number allocated to the HII regions by the FOF algorithm

5.2.1. Recombining regions

The most striking feature of SB models (and to a lesser extent S models) is the presence of recombining HII regions, tracked as connection-less branches in the merger tree. Recombination can be driven by two main factors: high density features or evolving sources. The evolution of the density is common to all experiments and the lack of such regions in H models indicates that it is unlikely to be the main origin of these peculiar regions. Nevertheless, a hint for this ‘density’ effect can be seen in the larger amount of such regions in the S50 model compared to S200, or their marginal presence in H50: higher resolution leads to higher contrasts and thus higher recombination rates. On the other hand, stellar sources are more prone to variation than ‘halo’ sources. First they exhibit some level of stochasticity, hence sources that turn off may not be replaced through an efficient renewal process in order to sustain some regions, whereas halo sources have by construction a continuous emission. It explains the lack of such regions in H models and their detection in S and SB models. Furthermore SB models have sources with a decreasing individual emissivity, leading to a typical scenario where strong early sources produce large regions that see their in-

ner ionizing engine becoming progressively weaker, or stars being replaced by weaker ones, eventually leading to recombinations. Combined to stochasticity, it can lead to regions that are being ‘dissolved’, potentially at several places within one region. Increasing the resolution tend to diminish the contribution of this type of regions in SB50 models: the differential boost applied to source is weaker than in SB200, hence decreasing the effect of inner exhausted engine and the stellar renewal is more efficient, leading to a production of ionized regions closer to a stationary regime. Looking at Fig. 10, it is interesting to note that in all the cases where they are detected, recombining regions stand for a small fraction of the total ionized volume: between $\sim 10^{-7}$ and $\sim 10^{-5}$ of the total volume of the box for the H50 and the SB200 model respectively. Therefore, even if recombining regions are good indicators of the behaviour of the source models, it can be seen that they correspond only to an almost negligible fraction in terms of volume and can be considered to some extent as marginal.

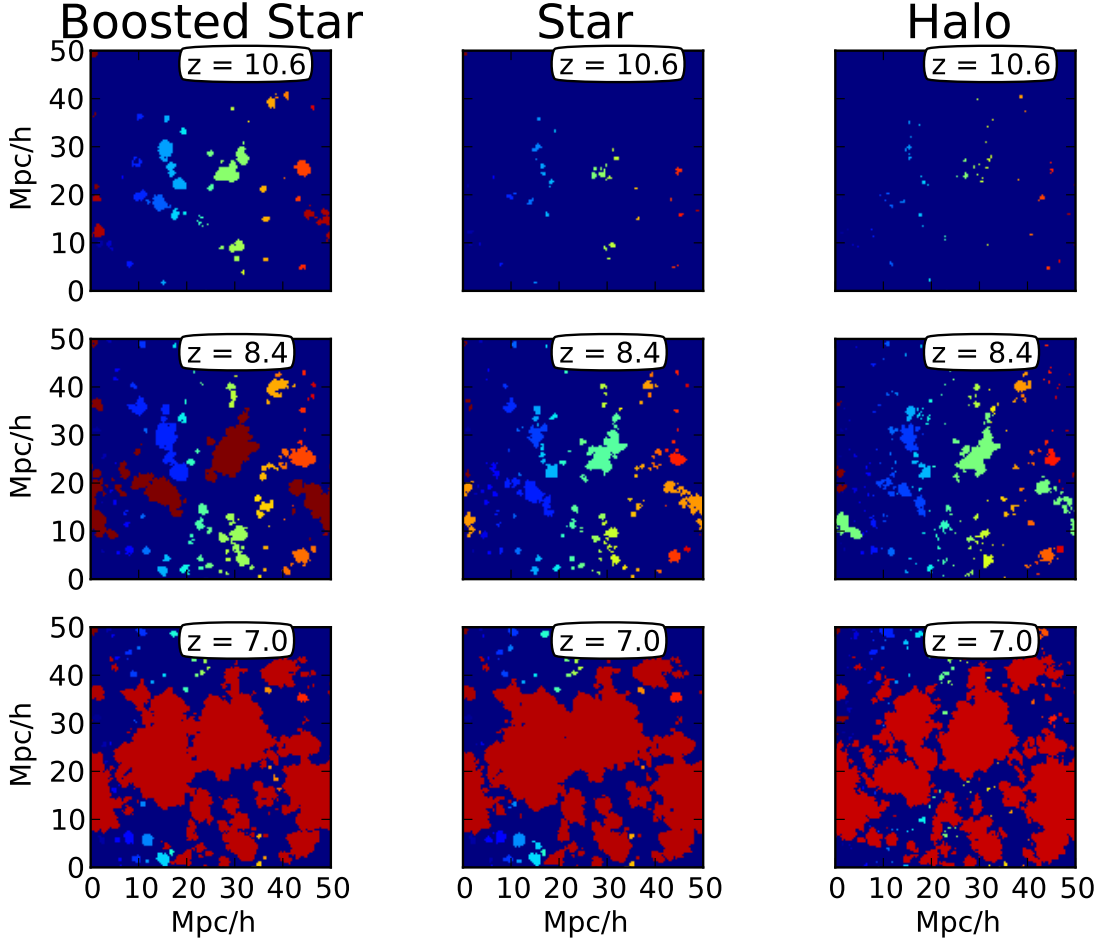


Fig. 7. Ionisation map for the three ionizing sources models for three distinct redshift for the 50 Mpc/h size box. The colours encode the different identification number allocated to the HII regions by the FOF algorithm

5.2.2. Regions in expansion

Expanding regions are detected as having one ‘parent’ only and distinguish HII regions that expand without additional event. In absolute number (see Fig. 8) their number peaks at z_{peak} and their proportion is always dominant until the very end of the reionization. Incidentally, it shows that the temporal sampling is high enough to generally track the initial expansion of individual regions. Also, the fact that such regions are still detected at the later stages suggests that even at the later stages of the percolation, not all the regions are involved in a global merging process: some regions still have room to experience stages of ‘quiet growth’ before eventually be part of the global ionized background. In terms of volume (see Fig. 10), expanding regions are the main contributors to the total ionized volume in every models until typically z_{peak} . This is not surprising since the expanding regions are naturally much greater in size than the new regions and are always dominant in number (see Fig. 8). Once the overlap start to be efficient, merged HII regions supersede the expanding ones in volume, as expected.

5.2.3. New regions

New regions (without parents in the tree) track the formation of new sites of emission, i.e. star or halos forming in areas distant enough of pre-existing ionized volumes. Of course, any source that appears within an ionized region because of clustering won’t contribute to this population. First, their proportion (and their absolute number) present regular ‘spikes’. The tree is constructed using a time sampling different than the sampling used to include sources in the radiative transfer calculation: the tree sampling frequency is low enough that between two snapshots at least a new generation of source has been included and new regions are thus detected. But this frequency is also low enough that regularly, two generation of new sources were included in the RT calculation between two snapshots, creating bursts of new regions. The presence of these spikes does not affect our analysis and conclusions.

Globally all experiments show an initial gradual decrease of the proportion of new regions. In the 50 Mpc/h experiments, this decline stays until the end of the reionization. It is related to a pile-up effect of pre-existing HII regions: until z_{peak} their number increase at a higher rate than the one of new regions. For instance, regions keep growing

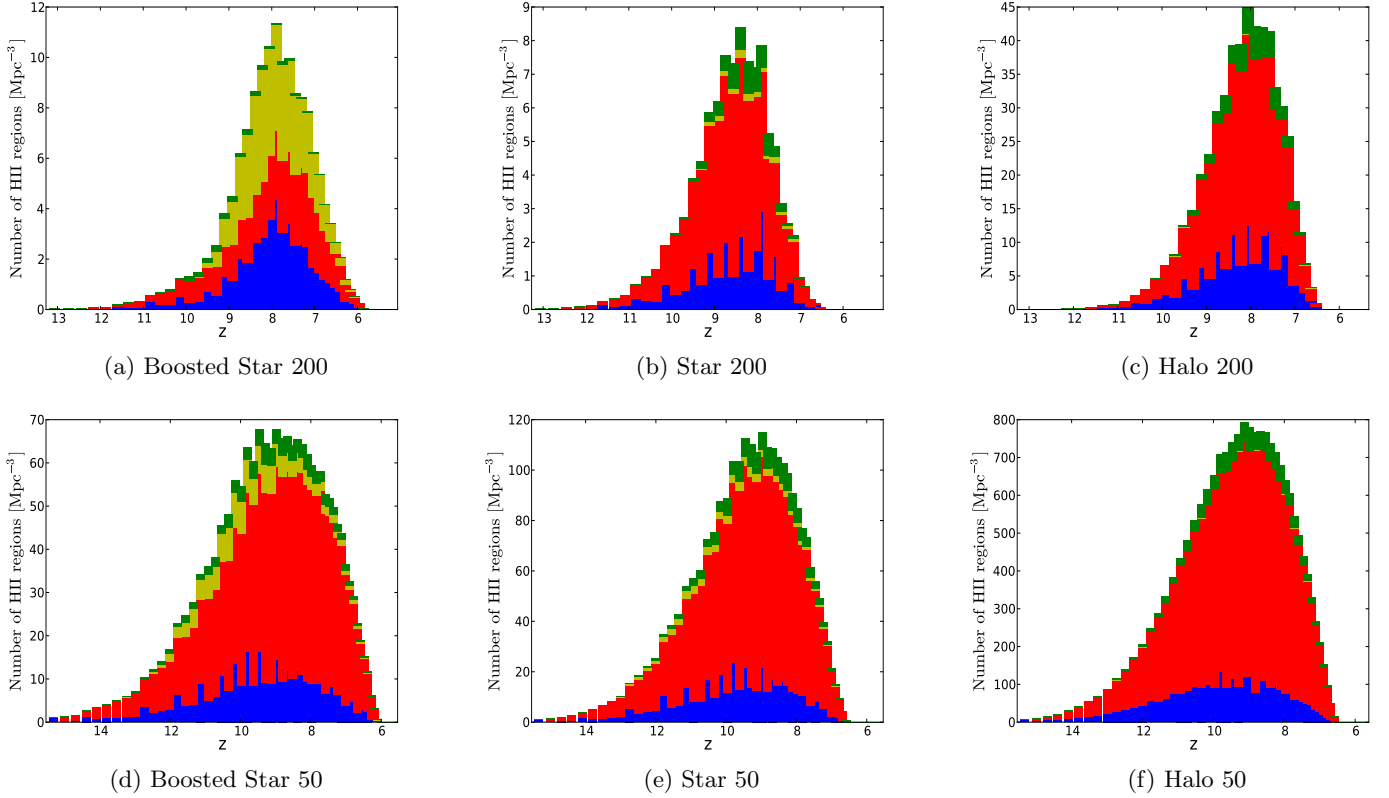


Fig. 8. Evolution of the number density of each kind of HII regions as a function of redshift for the three models of ionizing sources and for both boxes of 200 and 50 Mpc/h. Panels (a), (b) and (c) respectively represents the distribution for the Boosted Star, the Star and the Halo model for the 200 Mpc/h box, while the panels (d), (e) and (f) are for the same models but for the 50 Mpc/h box. The colours stand as follow: Blue for the new HII regions, Red for the expanding regions, Yellow for the regions that will recombine and Green for the regions resulting from mergers.

without efficient merging over several generation of new HII regions: it increases the number of pre-existing regions and decrease mechanically the proportion of the new ones at a given moment. After z_{peak} , the proportion of new regions increases in 200 Mpc/h experiments and arguably remains constant in 50 Mpc/h ones. By construction the overall number of ionized sites decreases in this ‘post-overlap’ period, indicating that among these sites, new regions suffer to a lesser extent of the percolation process. Hence while the destruction rate of pre-existing HII regions is important, new stars or halos manage to appear in neutral areas, sustaining (in the 50 Mpc/h box) or even increasing (in the 200 Mpc/h box) the relative contribution of the new regions. This increase of the contribution of new regions seen in S200 and H200 is indicative that the destruction of pre-existing regions is more sudden than at higher resolution: it was hinted in Fig. 8 where the post z_{peak} evolution is smoother at high resolution or in Fig. 4 where the average ionized fraction exhibits a sharper evolution at reionization. Regarding this sharper evolution, let us emphasize that a more accurate tuning of the source emissivity could have increased the matching of the reionization history of the H and S models and may be the origin of this difference between high and low resolution. It may also be the result of a different behaviour in the propagation of fronts at low resolution (with faster fronts and weaker shielding), leading to a more radical percolation in the 200 Mpc/h simula-

tions than in the 50 Mpc/h boxes. Finally, let us mention that the presence of a strong recombining component in the SB200 model lead to a totally different evolution of the new regions contribution: it remains broadly constant at all redshifts with a weak dip at $z \sim 10$. Without this recombining regions, it would also exhibit a rising relative weight of new regions, albeit starting much earlier than z_{peak} .

Regarding their volume fraction (see Fig. 10), these newly detected regions only represent a maximum of $\sim 10^{-4} - 10^{-3}$ of the total volume even if there is a sizable number of this kind of regions detected. This is understandable because of their very nature: new regions are by definition expected to be small, since they just appeared and their number cannot compensate this effect. Interestingly, the total volume occupied by the new regions remains broadly constant until overlap : it indicates that even though sources increase in number with time (and thus the potential number of new regions) it competes with the gradual decrease of available neutral volume, these two effects ‘conspiring’ to keep constant the volume imprint of the new patches on the network of HII regions.

5.2.4. Regions resulting from mergers

These regions have more than one parent and result therefore from the merger of several regions. They track the coalescence of pre-existing regions into larger ones and even-

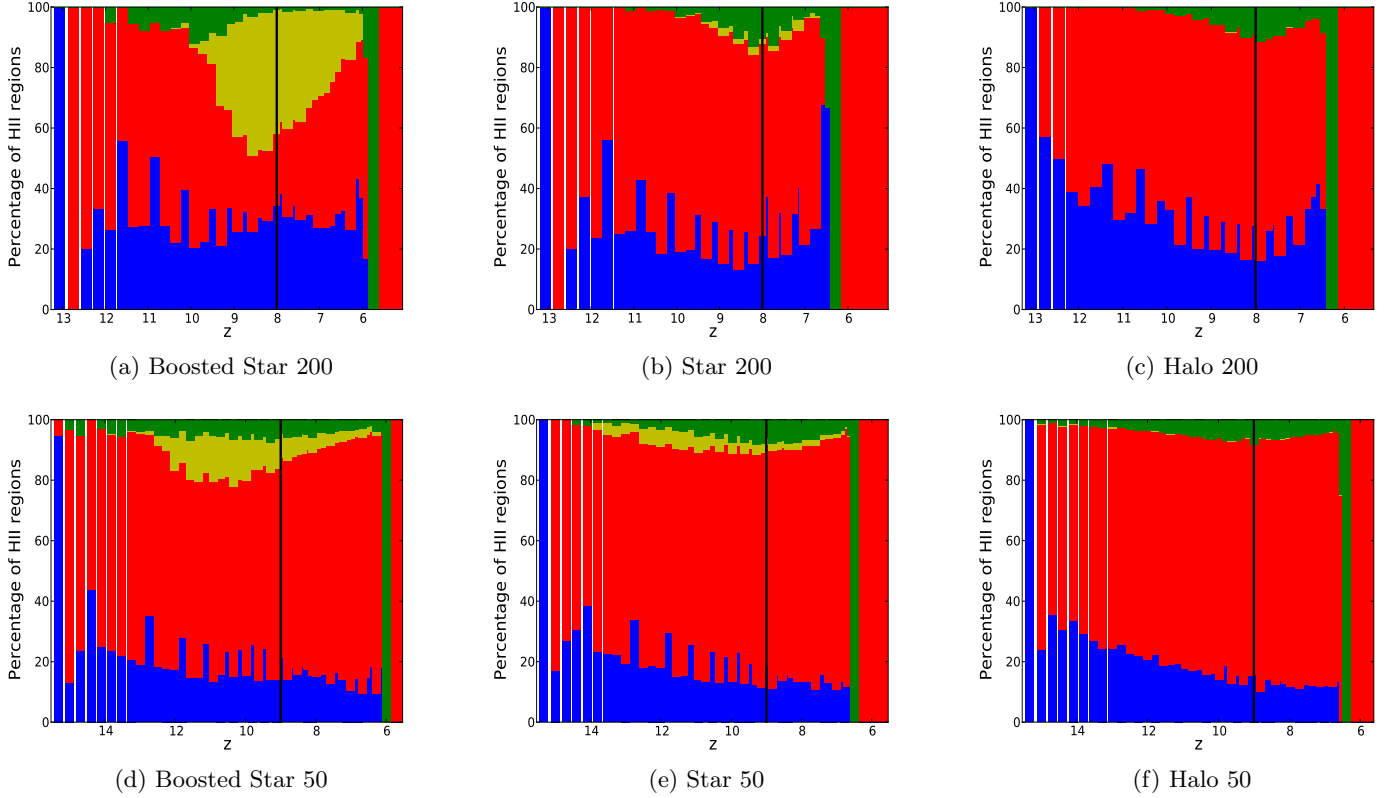


Fig. 9. Evolution of the proportion of each kind of HII regions as a function of redshift for the three models of ionizing sources and for both boxes of 200 and 50 Mpc/h. Panels (a), (b) and (c) respectively represents the distribution for the Boosted Star, the Star and the Halo model for the 200 Mpc/h box, while the panels (d), (e) and (f) are for the same models but for the 50 Mpc/h box. The colours stands as follow: Blue for the new HII regions, Red for the expanding regions, Yellow for the regions that will recombine and Green for the regions resulting from mergers. The black vertical line shows the peak of the absolute number of HII regions: z_{peak} .

tually track the final overlap into a single large HII region at the end of reionization. This last stage can be seen in all models where there exist a late snapshot where 100% of the detected region result from mergers, an indication of the ultimate merger. S and H model present similar evolutions for the merger populations. Their proportion is ‘co-incidentally’ maximal at z_{peak} : as the number of ionized patches gets larger, a larger fraction of them is involved in mergers, indicating a ‘crowding’ or clustering effect where a smaller volume is available for expansion as the number of HII regions increase. Later on, for $z < z_{\text{peak}}$, the proportion of mergers decreases indicating that only a subset of the ionized regions do actually merge, potentially only one that would phagocyte the others, reducing the overall number of individual regions until the end. Hence the peak of mergers fraction could be seen as the rise of one or several dominant regions and this rise appears when the number of individual region is maximal.

Comparing the two resolutions, it can be noted that mergers are concentrated over a smaller range of redshifts at low resolution whereas merger can be detected at a significant level during the whole experiment in the S50, H50 and SB50 models. Firstly, it can be the consequence of the slightly more extended history of reionization in 50 Mpc/h simulations, already mentioned regarding the $\langle x(z) \rangle$ trends (see Fig. 4). Furthermore, sources and individual regions

are more numerous at any time and in a smaller volume, in favor of a more generalized contribution of mergers over a large range of redshifts.

Finally, it should be noted that the SB200 model presents an early peak in the fraction of merger, at $z \sim 10$ instead of $z \sim 8$ for all the others experiment, with an almost zero contribution later on, even though the absolute number of regions manage to decrease at some point. It suggests that the onset of the global percolation started earlier, due to early large HII regions induced by the large initial boost of this model, and created a single region that monopolize the merger process. Interestingly, in this case z_{peak} occurs later, indicating that while this main region grows, there remains a significant amount of neutral volume to host the apparition of new regions.

Finally, Fig. 10 clearly indicates that these merger regions dominate the fraction of the ionized volume for $z \leq z_{\text{peak}}$. It was not obvious given that their number density is always the lowest contribution (cf. Fig. 8). It is indicative that few of these regions produce a network that dominate the ionized volume and/or that such regions are individually very large, as one would expect from them being the result of several mergers. This point is assessed in greater detail in the next sections.

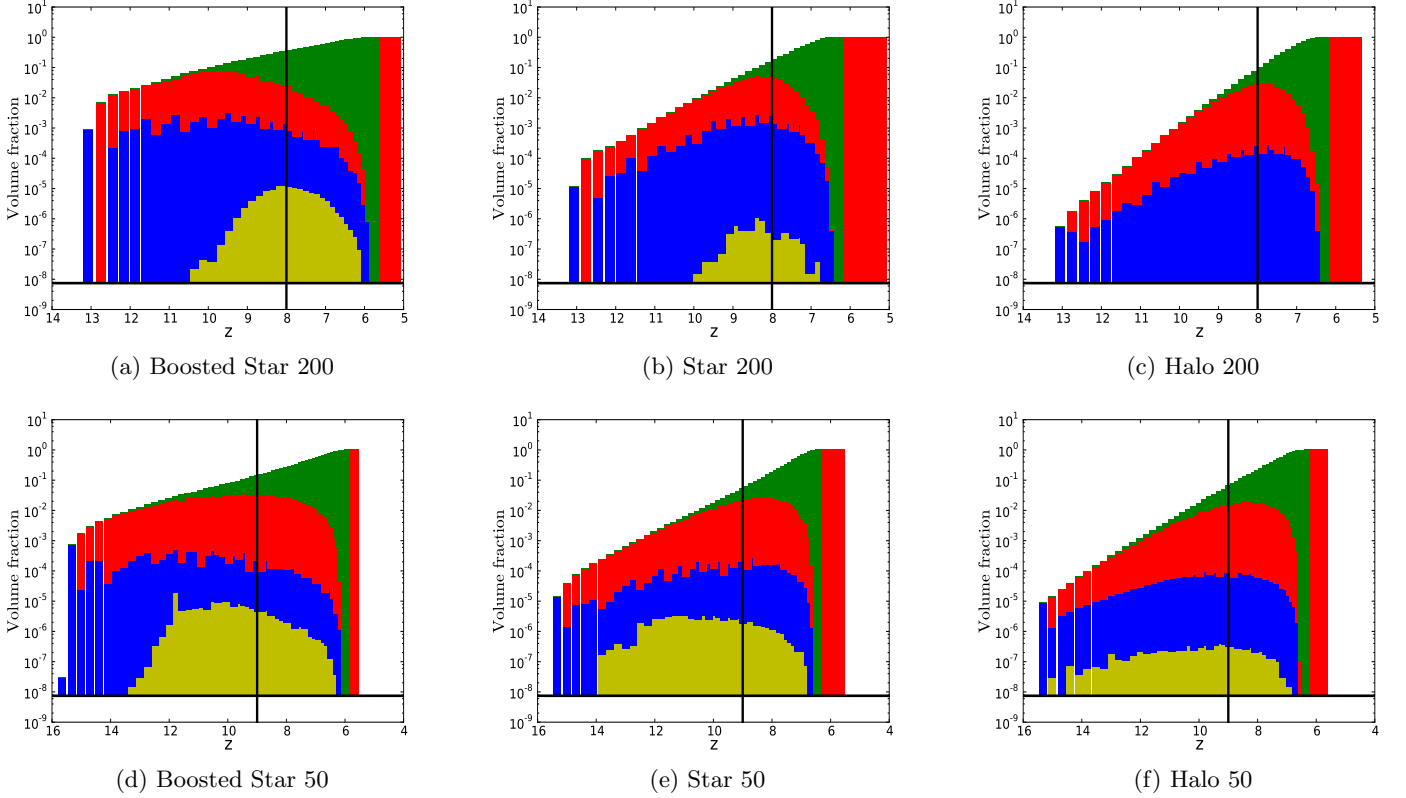


Fig. 10. Evolution of the volume fraction of each kind of HII regions as a function of redshift for the three models of ionizing sources and for both boxes of 200 and 50 Mpc/h. Panels (a), (b) and (c) respectively represents the distribution for the Boosted Star, the Star and the Halo model for the 200 Mpc/h box, while the panels (d), (e) and (f) are for the same models but for the 50 Mpc/h box. The colours stands as follow: Blue for the new HII regions, Red for the expanding regions, Yellow for the regions that will recombine and Green for the regions resulting from mergers. The black vertical line shows the peak of the absolute number of HII regions: z_{peak} and the black horizontal line shows the volume fraction of one cell of the grid.

5.3. Sizes of HII regions

5.3.1. Sizes distribution with redshift

Fig. 11 shows the evolution of the distribution of the HII regions radii at each instant as a function of redshift for the 200 and 50 Mpc/h box. Like Friedrich et al. (2011), we compute the volume of the HII region and then we derive the effective radius corresponding to a sphere of equal volume through the following expression $R = [3/(4\pi)V]^{1/3}$. The white dashed curve shows the radius evolution of the last HII region which remains at the end of the simulation. With the help of the merger tree we follow this region back in time and calculate the radius of its main progenitor at each instant. In addition the solid white line represents the evolution of the average radius of HII regions as a function of redshift. The color code in the distributions is made so that the brightest red cell contains only a *single* HII region. Other red tones up to the brightest green designate cells populated by a couple HII regions up to a value corresponding to half the maximal value of the distribution. Finally the purple tones (from the darkest to the brightest) encode the largest values of the distribution.

Typically, each distribution seems to trace the underlying ionizing source prescriptions related to the model considered. The Star model has a constant star emissiv-

ity with redshift. This is reflected in the radii distributions where ionized regions are concentrated with a constant radius about $r \sim 4$ Mpc/h over the whole range of redshift in the 200 Mpc/h box. We find a gap at about $r \sim 2$ Mpc/h in the size distribution where there are only a few regions with radii under this constant radius. This would indicate that the time sampling used here cannot entirely capture the fast tracks followed by the HII regions in the radius-redshift space with strong inner sources. This effect is attenuated for the 50 Mpc/h box (that contains typically weaker sources and HII regions with smaller growth rates) where we observe a more continuous distribution even if there remains a typical cutoff radius of $r \sim 0.4$ Mpc/h, with smaller occupation numbers at low values.

On the other hand, the Halo model implies that each of them has an emissivity proportional to its mass. As these masses cover a large range, we find a large range of radii for the resulting HII regions in the distribution of the 200 Mpc/h box. The regions are concentrated in larger intervals of radii than in the other models that typically trace the underlying mass range of halos. The shape of the distribution is almost the same when we consider the 50 Mpc/h experiment, with smaller regions as expected since smaller halos are available at higher resolution.

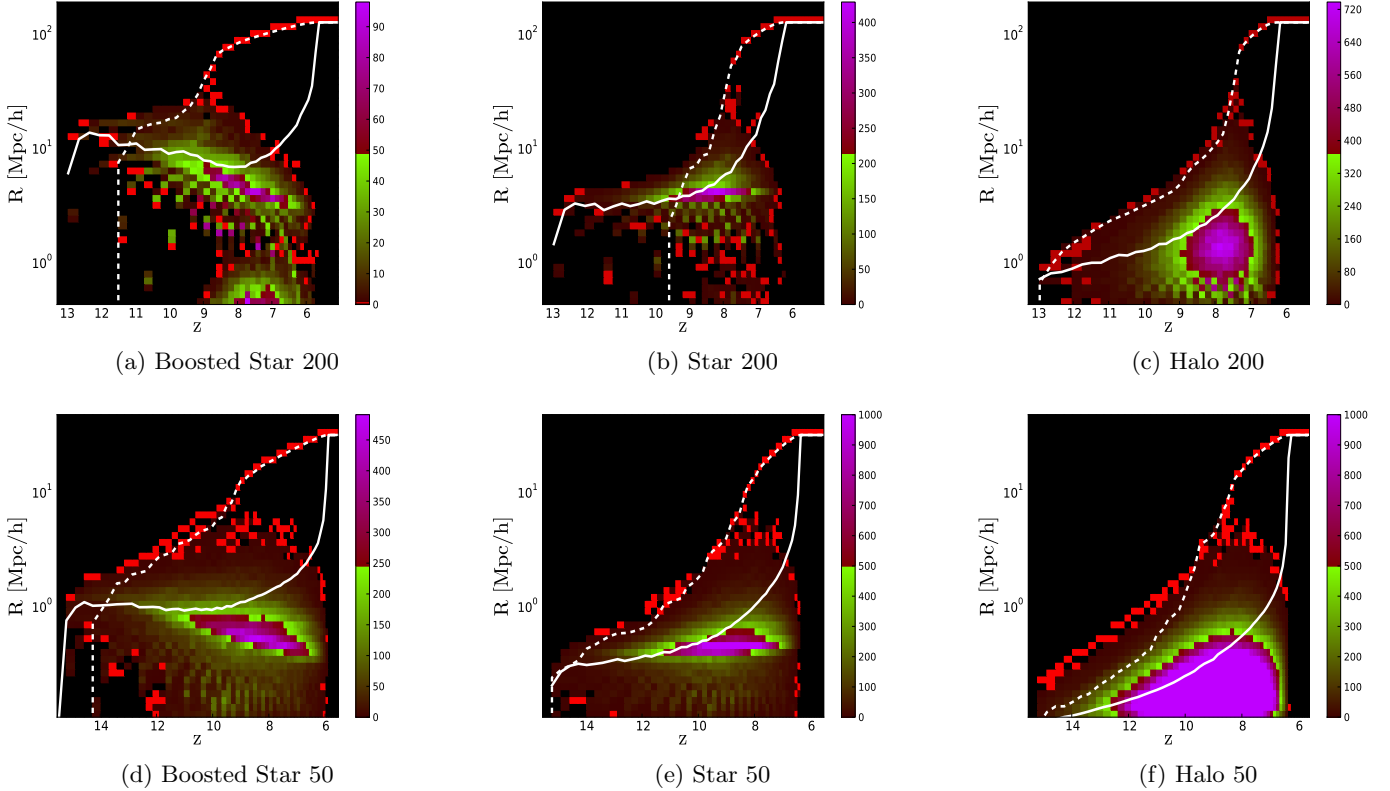


Fig. 11. Evolution of the HII regions radius distribution as a function of redshift for the three models of ionizing sources formation and for both boxes of 200 and 50 Mpc/h. Panels (a), (b) and (c) respectively represents the distribution for the Boosted Star, the Star and the Halo model for the 200 Mpc/h box, while the panels (d), (e) and (f) are for the same models but for the 50 Mpc/h box. The color code stands as follows: the brightest red cells represent the location in the distribution populated by *a single* HII region, other red tones up to the brightest green cells spans distribution densities from a couple HII regions up to a value corresponding to half the maximal value of the distribution. Finally the purple tones (from the darkest to the brightest) encode the maximal values. The evolution of the average radius and the evolution of the radius of the main region are shown respectively with the solid and dashed white lines.

Finally, the boosted Star model has a boost for the star emissivity that decreases with redshift. Indeed the distributions show, at early times, large HII regions detected without small counterparts. This gap would be the result of the very powerful boost for ionizing sources at high redshift combined to the time sampling of the simulation which allows to detect only regions when they have a large radii early in the reionization. Then we can observe a decreasing gradient for the typical radius of the regions as the boost for the emissivity decreases with time. Surprisingly we find a bimodal distribution from a redshift of $z \sim 9$ until the reionization at $z \sim 6$. Some HII regions are concentrated with radii below or under ~ 1 Mpc/h with a gap in the distribution for this value. To a lesser extent, the same effect could be seen in the Star 200 model. This regions with radii under ~ 1 Mpc/h could be the recombining regions that we have found in figure 9. This could also be combined with the fact that around these redshifts the boost emissivity falls down under a certain value. Then, the time sampling of the simulation would become fine enough to detect some new or expanding regions with these radii. We will further investigate this in the following section 5.3.2. For the SB50 model, this bimodal distribution disappears: a weaker boost amplitude and variation combined to a more

stationary production of stars promotes a better tracking of regions sizes as they grow and reduce the contribution of recombination, as seen earlier.

Considering again the S and H models, for both box sizes, it is interesting to note that the S model produce a truncated version of the H one. Above the cutoff radius (0.4 Mpc/h (resp. 4 Mpc/h) in the S50 (resp. S200)) the S and H distributions are quite similar. At smaller radii, S has less objects than H. It is indicative that there is a scale above which the clustering of halos combined to their own mass-proportional emissivities produce a similar radii distribution to the one provided by the clustering of stellar sources and their own constant emissivity. At smaller scales, the stellar sources are too scarce to reproduce the regions created by halos, resulting in overpowered individual sources with large radii. At larger scales the two approach produce equivalent size distributions and with an appropriate calibration, hydrodynamically created sources can match the halo result. It should be noted that this typical scale appears at smaller values in S50 models as sources are more numerous and are less prone to stochasticity and therefore converges toward the halo model behavior on smaller volumes.

Finally, all the experiments present a single main HII region that dominates in size. It appears at $z \sim 8$ in the S200 and H200 models and much earlier ($z \sim 9$) in the SB200. As suggested by the previous study on merger populations, it is likely the consequence of the boost that creates early large regions that merge at high z to give the dominant one. Interestingly the dominant region of the late reionization is not dominant in size at every redshift: this is indeed the case for the H200 model and to some extent for the S50 model too, but in all the other case this region started as a non special one inside the population, at least from the ‘radius’ point-of-view. Furthermore, the first progenitor of the dominant region is among the very first ionized regions of the H200 and H50 models but appears later in the S and SB experiments. It is noteworthy that even though we argued that S and H model produce similar populations (for regions larger than the cutoff radius) it seems that for individual cases, differences can persist, especially for the buildup of the dominant region. As we will see in next sections, the channel through which this specific region grows (through expansion rather than merger) also differs as hinted by the difference between the smooth evolution of the dominant region of H models and the sharp, kinked and late rise of its equivalent in e.g. the S200 model.

5.3.2. Radius distribution of the different kind of HII regions

Fig. 12 presents the size distribution for each kind of HII regions as a function of redshift for all three models and for both 200 and 50 Mpc/h boxes. Here we show the same distribution seen in figure 11 but by plotting the contours related to each type of HII regions that we can discern. The colour code stands as follows: Blue corresponds to the new HII regions, red to the expanding ones, green to those resulting from mergers and yellow to regions that will recombine. Once again we show the evolution of the average radius of the region with the black curve and the evolution of the radius of the last HII region with the black dashed curve as in the figure 11.

Initially, we observe that each kind of HII region occupies a dedicated range of radii in the whole distribution for all models and for both 200 and 50 Mpc/h box sizes. As expected new regions occupy the smallest range of radii while the regions resulting of mergers are those which populate the top of the distribution. The expanding HII regions are in the middle with radii greater than the new ones and smaller than those that will merge. We can also see in each model that the peak of the distribution of the figure 11 correspond to a radius range that is simultaneously covered by the three kinds of HII regions. Alternatively, we could have imagined a clear separation between the different range of radii covered by the different kind of HII regions instead of the observed overlap of the different distributions. This tells us first that the time sampling here allows us to detect HII regions with same radii but belonging to different kind of HII regions with different paths in the radius-redshift space. It also indicates that the peak of the radii distribution must be understood as the most likely radii of detection, with a mix of HII regions at different stages of their evolution (newborn, growing or merging).

Interestingly, for each kind of regions, we find the properties of the underlying ionizing source models in the evolution of the radius distribution with redshift. In other words the $R(z)$ distribution for the size evolution of each kind of

regions as function of redshift is dictated by the $R(z)$ distribution of the new regions and is propagated to the other kind of regions. We thus can see a similar R - z relationship for the expanding region and those resulting from merger with a simple translation. In the Star models S50 and S200 the new regions appear with a relative constant range of radii during the whole reionization; again, it reflects the typical constant emissivity of the stars appearing during the whole simulation combined to the time sampling used here. The expanding regions and those resulting from mergers also show this constant radius range but translated to greater radius ranges. The S50 allows to track smaller new regions thanks to its higher resolution in terms of sources with smaller individual emissivity: as a consequence all subsequent types show smaller typical radii than in the S200 model.

The H200 model presents new regions that appear with sizes more distributed than in the S50/S200 models and typically result from the mass range of the dark matter halos that are assumed as ionizing sources. Then the expanding regions cover a much greater radius range compared to the two other models and we find the same trend for the regions resulting from mergers. The last point indicates that the merger process is not dominated by a few large regions as in the two other models but also involves sets of small HII regions. In the H50 model the mixing is more pronounced and the ranges of radii covered by each kind of regions overlap. Highly clustered regions are more represented at high resolution where dense set of small halos with small regions can also merge. In H200, mergers occur at later stage of radii evolution, in a more homogeneous distribution of halos at low resolution.

Finally, SB200 shows that new regions appear with decreasing radii as reionization progresses and as the boost for the star emissivity decreases. The expanding regions and those resulting from merger show the same R - z decreasing trend, seeded by the new regions population properties. It should be noted that at some point ($z < 9$), new regions can be detected at small radii: the declining boost leads to individual regions that appear with smaller size and growth rate, increasing the likelihood to spot them at small radii. A weaker R - z slope is found in the SB50, as a consequence of a smaller boost correction at higher resolution. As expected, new regions with small radii are found earlier (for $z < 12$) and globally share a greater number of broad features (like the range of radii of each type) with the S50 model.

Let us finally focus on the HII regions that recombine in the size distributions of each model. We find as expected in section 5.3.1 that regions that will recombine are those with radii below the radius of ~ 1 Mpc/h in both SB and S models and at both resolution. As already mentioned, the recombination is driven either by density or a modification of the sources. In the case of SB models, it is fairly obvious that strong early sources create large HII regions that may be unsustainable by later generation of sources which are individually weaker by construction of the boost. Furthermore, the boost guarantees a global convergence but locally a strong early source can be replaced by too few weaker later sources, especially if the source renewal is subject to stochasticity. Once sources become too dim, it leads to the fragmentation of regions and recombinations at small scales. S models also present some degree of recombination, even though they do not contain declining sources. These recombinations can be explained by local dense patches and

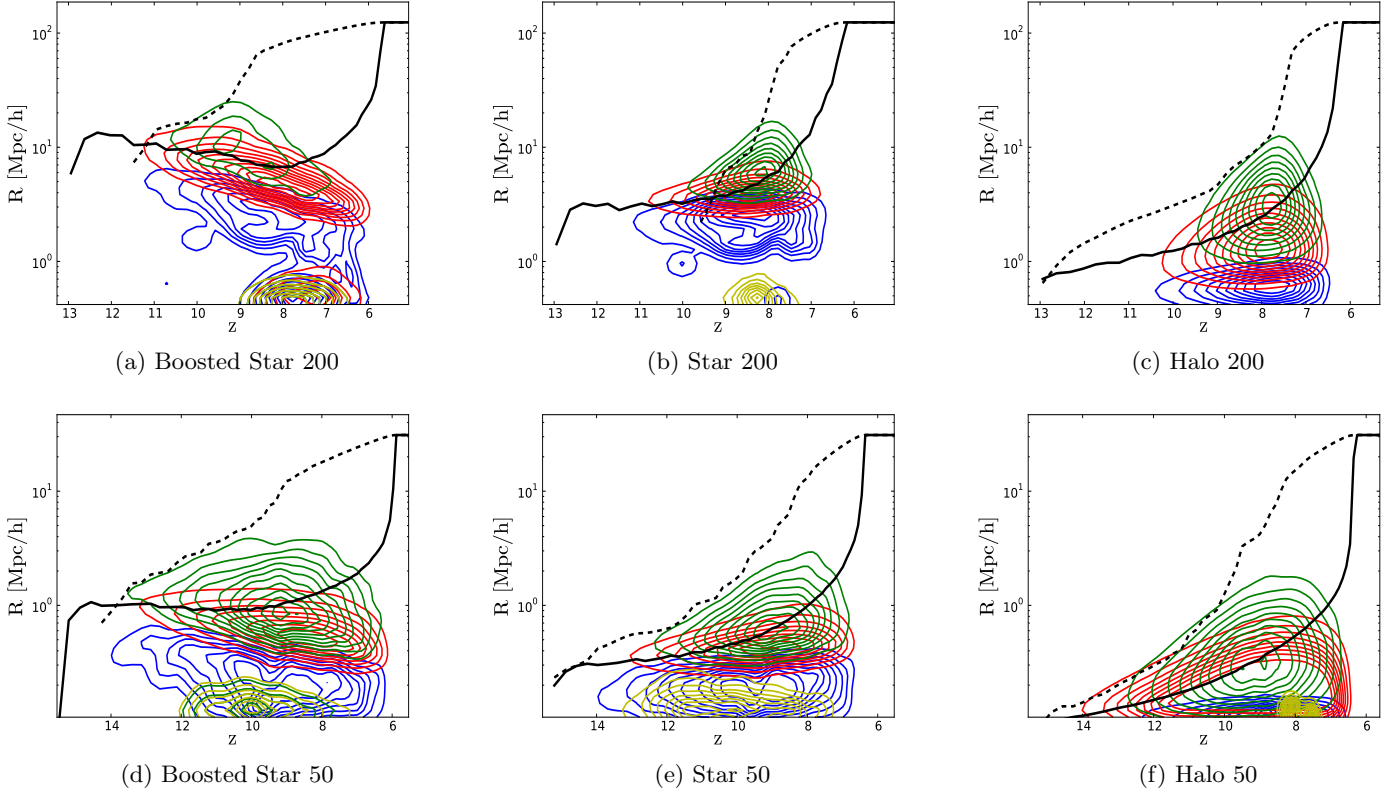


Fig. 12. Evolution of the radius distribution of each kind of HII regions as a function of redshift for the three models of ionizing source formation and for both boxes of 200 and 50 Mpc/h . Panels (a), (b) and (c) respectively represents the distribution for the Boosted Star, the Star and the Halo model for the 200 Mpc/h box, while the panels (d), (e) and (f) are for the same models but for the 50 Mpc/h box. The colours stand as follows: Blue for the new HII regions, Red for the expanding regions, Yellow for the regions that will recombine and Green for the regions resulting from mergers. In addition the solid and dashed black lines represent respectively the radius evolution of the main region and the evolution of the average radius for the HII regions.

it could be supported by the fact that such regions only appear at later time ($z < 9$) in the S200 model, when local clustering is high enough. Furthermore, in both S50 and SB50 models, these regions can be found over extended period compared to their 200 Mpc/h equivalent, related to the fact that dense patches that trigger recombination are more likely to be found at high resolution.

5.4. Mergers of HII regions

5.4.1. General evolution of the merger process of HII regions

Fig. 13 is restricted to regions that have more than one parent, i.e. that result from mergers. It presents the redshift evolution of the distribution of the number of parents. It can be seen as a measure of the patchiness or granularity of the overlapping process and is also a first indication of the inner complexity of the regions: an ionized volume that result from tens of progenitors is shaped (like e.g. the front propagation, its growth rate, or the inner distribution of UV flux) by the different properties of at least tens of sources whereas an HII region coming from a binary merger is likely to be, maybe naively, more straightforward to relate to its inner sources. In addition, the solid white line in figure 13 shows the evolution of the average number of parents and

the white dashed line stands for the evolution of the number of parents for the last remaining region at the end of the simulation. Again, with the help of the merger tree we follow this region back in time and evaluate its number of parents at each instant. The color code in the distributions is identical to the one used in the figure 11.

Firstly, in most of the models the mergers between regions operates in a binary-tertiary manner as seen with the peak at $\sim 2-3$ in the distributions. It is essentially an indication that the temporal sampling of the tree is fine enough to track individual mergers whereas a coarser grained sampling would have presented a typical larger value. One exception is the H50 model, where clearly such mergers are missing from $z \sim 10$ to $z \sim 7$. In this case, the abundance of clustered individual regions at high density is much higher than in other models and leads to multiple mergers during a single time step for a given region.

Then, in every model we find the emergence of a single region which is the result of more mergers than other regions. In the S200 and H200 models, this region appears at $z \sim 8$ and earlier in the SB200 one, at $z \sim 9$. The same discrepancy can be found at higher resolution with a formation at $z \sim 9$ for the S50 and H50 models and $z \sim 10$ in the SB50. Interestingly, this merger-dominant regions appear at the same moment as the radius-dominant region discussed

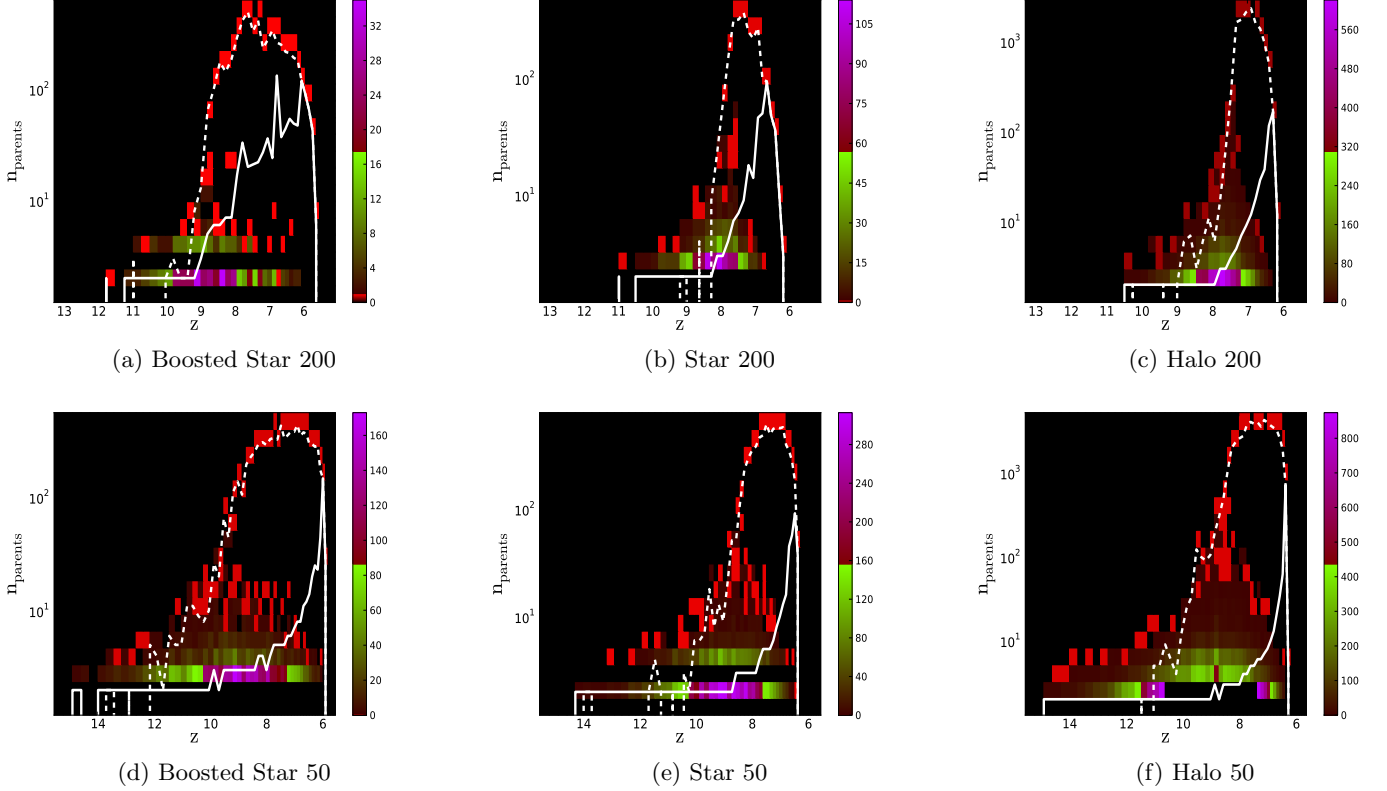


Fig. 13. Distribution of the number of parents for the HII regions resulting from merger as a function of redshift for the three kinds of ionizing sources and for both box sizes of 200 and 50 Mpc/h. Panels (a), (b) and (c) respectively represents the distribution for the Boosted Star, the Star and the Halo model for the 200 Mpc/h box, while the panels (d), (e) and (f) are for the same models but for the 50 Mpc/h box. The color code stands as follows: the brightest red cells represent the location in the distribution populated by *a single* HII region, other red tones up to the brightest green cells spans distribution densities from a couple HII regions up to a value corresponding to half the maximal value of the distribution. Finally the purple tones (from the darkest to the brightest) encode the maximal values. We represent in addition the evolution of the average number of parents and the evolution of the number of parents of the main region respectively with the solid and dashed white lines.

in the previous section. In Fig. 13, the white dashed line shows the evolution of the number of parents of the radius-dominant region and unsurprisingly it matches the path of the merger-dominant one. Thus, a moment exists when an HII region begins to monopolize the merger process in the box. Then the region grows faster by successive mergers and will quickly dominate other regions in terms of size. From this instant (called z_{BKG}), the probability that a location is part of the global UV *background* instead of being irradiated by a local source increases and can be considered as the onset of the overlapping process. This is typically the moment when on average the local information about the reionization process start to be lost to the benefit of a single reionization history.

Size is an important factor for regions to get high numbers of progenitors as a larger volume naturally promote encounters with distant ionized patches. However it can be noted that the radius-dominant region is only one among the merger-dominant regions. Clearly the distribution shows regions with larger number of progenitors and this is especially the case for H200 and H50 models: the high density of sources and their clustering can induce high merger rate in smaller volumes. More generally, high reso-

lution experiments present greater merger rate thanks to a higher number of sources and higher local clustering. Also H models can achieve number of progenitors that are ten-fold greater than the S and SB equivalent as another consequence of large number of halos. The two stellar models differ also in the number of regions with a large number of progenitors: close to z_{BKG} , S models present clear detection of regions with a number of progenitors close to those found for the radius-dominant one (10-50 progenitors), whereas in SB models such regions are hardly found. It indicates that the early buildup of a dominant region in the SB model tends to prevent the formation of separate regions that aggregate large number of sources on their side, probably because they were incorporated early in this dominant volume. At higher resolution the discrepancy is weaker, but in the S50 models, the dominant region share with more other regions the property of having a large (> 10) number of progenitors.

5.4.2. Growth of the main HII region

We aim with this section at understanding how the dominant region leads to a loss of information about the expan-

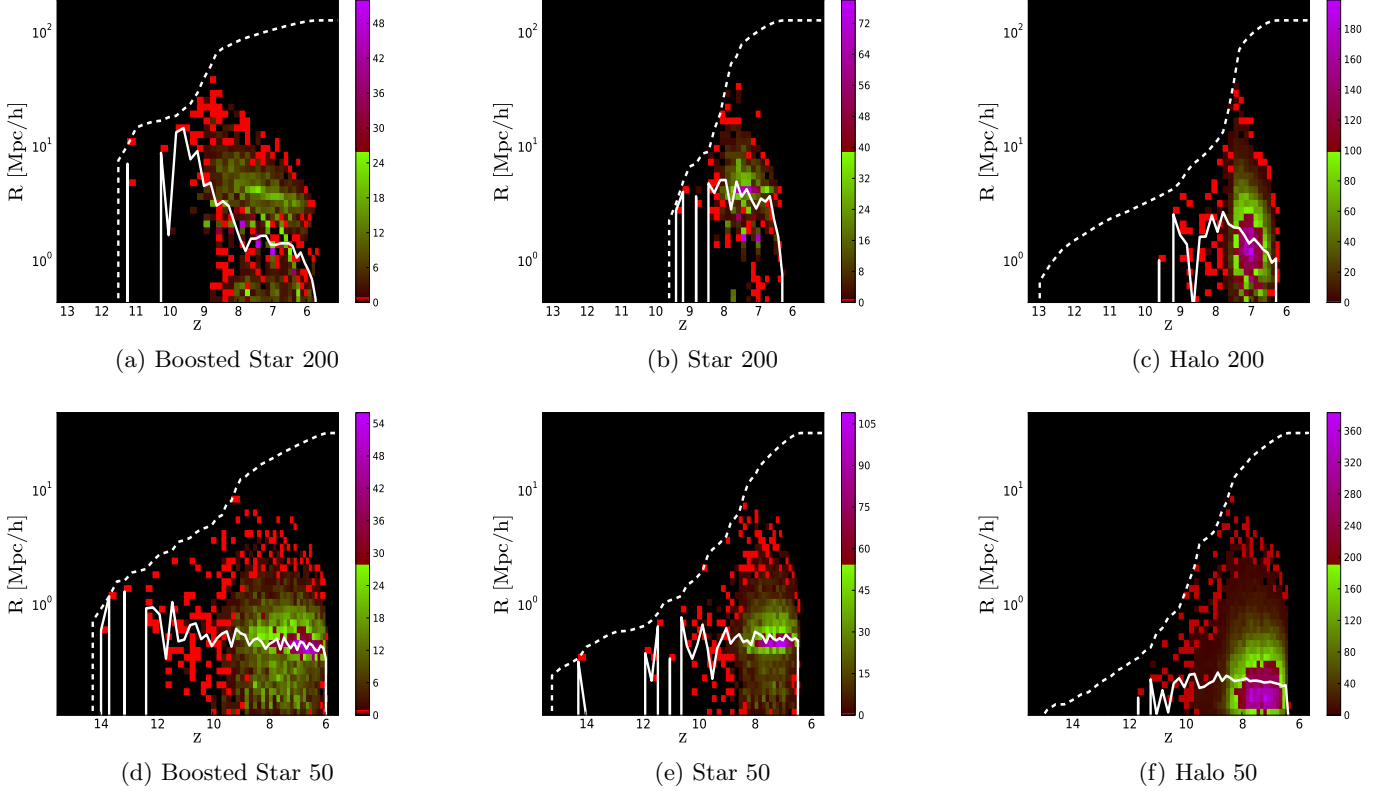


Fig. 14. Distribution of the HII regions sizes for the regions that merge with the dominant region as a function of redshift for the three kinds of ionizing sources and for both box sizes of 200 and 50 Mpc/h. Panels (a), (b) and (c) respectively represents the distribution for the Boosted Star, the Star and the Halo model for the 200 Mpc/h box, while the panels (d), (e) and (f) are for the same models but for the 50 Mpc/h box. The color code in the distributions is made so that the brightest red cell contains only a single HII region. Other red tones up to the brightest green designate cells populated by a couple HII regions up to a value corresponding to half the maximal value of the distribution. Finally the purple tones (from the darkest to the brightest) encode the largest values of the distribution. The evolution of the average radius for the regions that merge with the dominant region and the evolution of the radius of the main region are represented respectively with the solid and dashed white lines.

sion process of others regions. By looking at the evolution of the properties of the regions that merge with the dominant one, we will evaluate how each model is resistant to the emergence of this main HII region.

Fig. 14 presents the evolution of the radius distribution for HII regions that merge with the radius-dominant one for all models and both 200 and 50 Mpc/h boxes. With the white dashed curve we show again the evolution of the radius of the dominant region and with the solid white line we show the evolution of the averaged radius of the HII regions that merge with it *only*. The color coding of the distributions is identical to the one used in the figures 11 and 13.

Immediately we see that, from a certain redshift, every model presents a radius distribution which is representative of the whole distribution of all HII regions, as discussed previously and shown in figure 11. In other words, from a certain moment onwards, the major part of the present HII regions are regions that will merge with the main region in the next snapshot. Thus this moment can be seen as the time when the main region imposes its domination. Then the later this moment appears, the longer the individual expansion process of ionized region can be tracked. In all

models and at both resolution this moment is broadly coincident with z_{BKG} : from this redshift any region (in terms of size) can be incorporated into the background.

It is also noteworthy to see how this main region is built before it begins to impose its domination. For instance both H50 and H200 models, the earliest stage of the buildup does not include any merger and the growth is purely driven by the inner source until $z=9.5$ (resp. 11.8) for the H200 (resp. H50) model. The equivalent region in the S200 model is detected later, with a large radius (~ 3 Mpc/h instead of 0.5 Mpc/h for H200) and incorporates immediately other regions with similar sizes. At higher resolution, the radius dominant region of S50 is always larger than its H50 counterpart and also incorporate other relatively similar region quite early (at $z \sim 14$ for instance). Clearly the stronger emissivity of individual stellar source produce larger progenitors for the S models than for the halo-based ones, promoting a merger-driven growth sooner. Meanwhile the SB models exhibits the expected and quite different evolutions for the dominant region: the large emissivity correction at early times creates a large dominant region at the earliest stages and it quickly incorporates other regions also ‘puffed up’ by the boost and therefore belonging to the same class

of large radius. In particular, SB50 present a whole succession of large regions, close to the white evolution track of the dominant one. For the latter, it implies that its radius is always larger than found in the S50 and H50 models and is driven by mergers much sooner. Previously, we found that high resolution tend to diminish the discrepancies of the SB model but in the current case, the higher level of clustering in the 50 Mpc/h box leads to a buildup scenario of the main region that is arguably more even more distinguishable compared to H and S models than in the 200 Mpc/h experiments.

6. Summary and conclusion

We developed a new methodology based on merger trees of HII regions to study the history of reionizations in cosmological simulations with full radiative transfer post-processed by the GPU-driven code ATON on RAMSES hydrodynamical snapshots. We applied systematically the technique in two sets of 200 Mpc/h and 50 Mpc/h simulations, where each set involved three kinds of source model:

- a halo model where halos act as sources of photons with an emissivity proportional to their mass,
- a stellar model where ‘star’ particles produced by the cosmological code act as the sources, with an emissivity corrected to complete the reionization at the same redshift as the halo model,
- a boosted stellar model, where the same ‘star’ particles are used but with time-dependent and decreasing correction on the emissivity to reproduce the converged emission of UV photons at each instant.

Corrections are necessary as the self-consistent production of ‘star particles’ by the hydrodynamical code is resolution-dependent and not fully converged at these resolutions. The emissivities were tuned to produce a similar ionization fraction evolution at both resolutions. HII regions were detected thanks to a FOF algorithm and linked along time within a merger tree structure.

Firstly, the three models present an evolution comparable in terms of global features. Indeed, the evolution of the optical depth and ionized fraction present similar shapes in all experiments.

The evolution of the number of present HII region reaches a maximum at the same similar redshift for all models and for both box sizes ($z=8.5$ and $z=9$ for the 200 and 50 Mpc/h experiments). However the study of the separate evolution of the different kinds of HII regions shows that the intense episodes of mergers occur earlier in the boosted Star model while it occurs later and at the same moment in the Star and Halo models in the 200 Mpc/h box. Also the boosted Star model is sensitive to recombination, due to sources unable to sustain the existing HII regions while only few recombinations occur in the Star model and no one in the Halo model in the 200 Mpc/h. In the 50 Mpc/h simulations, episodes of mergers are similarly distributed in the three models, whereas increased densities are likely to produce the larger population of recombining patches in the Star experiments.

We also investigated the evolution with redshift of the size distribution of HII regions. All models present the emergence of a main region in size from a certain redshift onwards. We also have found that the evolution of the radii

distribution is typically related to the evolution of the ionizing source emissivities in each model: a large dispersion of possible radii with small structures in the halo-based models, a similar distribution for the stellar model with a lack of small regions due to stronger and sparser emitters and a distribution strongly skewed toward large regions at early times in the boosted stellar experiments. The discrepancies decrease at higher resolution but remain, especially for the last model. We have then be able to show that this radius-redshift correlation, imprinted in the distribution of new regions is somehow memorized and kept in the distribution of growing and merging ionized patches.

The evolution of the number of parents involved in the percolation of HII regions has also been studied. In all experiments, merger-dominant (with 10 or more progenitors) regions exist and among them one corresponds to the radius-dominant one and drives the reionization. Its domination is delayed in both halo and stellar model compared to the boosted one. As an illustration, we investigated the size distribution of HII regions assimilated by the main one and found that indeed it becomes representative of the whole distribution first in the boosted stellar model, than in the star model and finally in the halo one. Hence individual reionizations can be tracked on a longer period in the two latter models. Increasing the resolution reduces again the differences, thanks to an increased convergence between the three types of sources.

Globally, we can say that the Star and the Halo models have similar histories even though the Star model lack small scale power and therefore local merger events. Meanwhile the boosted Star model presents its own reionization history, where we see the early emergence of a dominant HII region in size that concentrates rapidly the merger process. On the other hand, both other models show individual growths for HII regions that can be tracked individually on a longer time and resist to the domination of the main region later on during the reionization. In the 50 Mpc/h box, when the spatial resolution is increased, the histories of the three models become comparable even if the boosted Star model still presents the domination of an early main region that concentrates the merger process.

Clearly, the large scale experiments show that the lack of convergence in the self-consistent formation of star particles leads to substantial differences in the HII regions properties and their evolution during the percolation process, even though they present satisfying properties regarding their global ‘integrated’ features. At higher resolution (corresponding to 50 Mpc/h boxes in our cases), we find that overall the discrepancies are reduced and can be seen as the result of smaller corrections applied to sources and a greater match between the halo population and the ‘stellar’ one. A question also remains on the quantitative impact of the rare ‘emitters’ more likely in the large boxes or the lack of density field variance in the 50 Mpc/h. Future experiments will allow to assert them even though we can predict e.g. that rare emitters should be relevant for the rise of the dominant regions whereas density field variance on small scales should impact the rate of local mergers.

We aim at systematically applying this technique in the future. For instance, it provides a reproducible analyzes framework to compare simulations, numerical techniques and the impact of physical ingredients on the morpho-chronology of the reionization. Furthermore, it puts the emphasis on individual HII regions, leading to an analyzes

in terms of *reionization-s* instead of *The Reionization*. In the context of galaxy formation, it may provide insights on the proximity effects which impacts the properties of the reionization as being seen by one or a group of galaxy (see Ocvirk et al. 2012 submitted).

Acknowledgments

The authors would like to thank B. Semelin, R. Teyssier, and H. Wozniak for valuable comments and discussions. This work is supported by the ANR grant LIDAU.

References

- Abel, T., Norman, M. L., & Madau, P. 1999, ApJ, 523, 66
Aubert, D. & Teyssier, R. 2008, MNRAS, 387, 295
Aubert, D. & Teyssier, R. 2010, ApJ, 724, 244
Baek, S., Di Matteo, P., Semelin, B., Combes, F., & Revaz, Y. 2009, A&A, 495, 389
Barkana, R. & Loeb, A. 2004, ApJ, 609, 474
Bond, J. R., Cole, S., Efstathiou, G., & Kaiser, N. 1991, ApJ, 379, 440
Choudhury, T. R., Haehnelt, M. G., & Regan, J. 2009, MNRAS, 394, 960
Courtin, J., Rasera, Y., Alimi, J.-M., et al. 2011, MNRAS, 410, 1911
Croft, R. A. C. & Altay, G. 2008, MNRAS, 388, 1501
Fan, X., Strauss, M. A., Becker, R. H., et al. 2006, AJ, 132, 117
Finlator, K., Özel, F., & Davé, R. 2009a, MNRAS, 393, 1090
Finlator, K., Özel, F., Davé, R., & Oppenheimer, B. D. 2009b, MNRAS, 400, 1049
Friedrich, M. M., Mellema, G., Alvarez, M. A., Shapiro, P. R., & Iliev, I. T. 2011, MNRAS, 413, 1353
Furlanetto, S. R., Hernquist, L., & Zaldarriaga, M. 2004a, MNRAS, 354, 695
Furlanetto, S. R., Zaldarriaga, M., & Hernquist, L. 2004b, ApJ, 613, 1
Gnedin, N. Y. & Abel, T. 2001, New A, 6, 437
Iliev, I. T., Ciardi, B., Alvarez, M. A., et al. 2006a, MNRAS, 371, 1057
Iliev, I. T., Mellema, G., Pen, U., et al. 2006b, MNRAS, 369, 1625
Kauffmann, G. & White, S. D. M. 1993, MNRAS, 261, 921
Kay, S. T., Pearce, F. R., Frenk, C. S., & Jenkins, A. 2002, MNRAS, 330, 113
Komatsu, E., Dunkley, J., Nolta, M. R., et al. 2009, ApJS, 180, 330
Lacey, C. & Cole, S. 1993, MNRAS, 262, 627
Lee, K., Cen, R., Gott, I. J. R., & Trac, H. 2008, ApJ, 675, 8
McQuinn, M., Lidz, A., Zahn, O., et al. 2007, MNRAS, 377, 1043
Mesinger, A. & Furlanetto, S. 2007, ApJ, 669, 663
Nagamine, K., Cen, R., & Ostriker, J. P. 2000, ApJ, 541, 25
Ocvirk, P., Aubert, D., Chardin, J., et al. 2012, MNRAS
Petkova, M. & Springel, V. 2009, MNRAS, 396, 1383
Prunet, S., Pichon, C., Aubert, D., et al. 2008, ApJS, 178, 179
Rasera, Y. & Teyssier, R. 2006, A&A, 445, 1
Razoumov, A. O., Norman, M. L., Abel, T., & Scott, D. 2002, ApJ, 572, 695
Shin, M., Trac, H., & Cen, R. 2008, ApJ, 681, 756
Springel, V. & Hernquist, L. 2003, MNRAS, 339, 289
Teyssier, R. 2002, A&A, 385, 337
Trac, H. & Cen, R. 2007, ApJ, 671, 1
Trac, H. & Gnedin, N. Y. 2009, ArXiv e-prints (astro-ph/0906.4348)
Willott, C. J., Delorme, P., Omont, A., et al. 2007, AJ, 134, 2435
Zahn, O., Lidz, A., McQuinn, M., et al. 2007, ApJ, 654, 12

Appendix A: FOF algorithm

A.1. Implementation

Our FOF algorithm proceeds by scanning all cells from the box and testing at each iteration the ionization status of the cell being explored. The algorithm simply proceeds as follow:

1	2	3	4	5	6	7
8	9	10	11	12	13	14
15	16	17	18	19	20	21
22	23	24	25	26	27	28
29	30	31	32	33	34	35
36	37	38	39	40	41	42
43	44	45	46	47	48	49

Fig. A.1. Illustration of the *friend-of-friend* algorithm (see Section A for details). White and black cells correspond to ionized and neutral cells respectively.

- If an ionized cell is encountered, it is given an ID corresponding to the ionized region being tested and the exploration of its neighbors begins :
 1. If a neighbor is not ionized, the cell is marked as visited. The parent cell is then reconsidered and the ionization status of the other near neighbors not already marked is tested.
 2. If the neighbor is ionized, it is given an ID corresponding to the ionized region being tested and we mark the cell as visited. The exploration of its own neighbors begins. The HII regions IDs diffuse from near neighbor to near neighbor.
- When all the neighbors of an ionized cell have been explored, we go back to its parent cell and continue the exploration of its near neighbor which were not previously visited. The identification stops when the starting cell is visited again and all its near neighbors are marked as visited.

The exploration of the cosmological box proceeds until another starting ionized cell is found and which is not already marked as visited. At this moment, a new identification starts with a new identification number.

In Figure A.1, an illustration of the algorithm in 2 dimensions is presented. In this figure, black cells correspond to neutral cell and white cells to ionized cells with a ionized fraction $x \geq 0.5$. In this example, 6 cells belongs to the same HII region, with numbers 17, 18, 25, 32 and 33 and all of them should receive the same identification number. Following the algorithm described above, the cells would be visited in the following order : 17-18-19-18-25-32-33-32-25-18-17. At this stage, the algorithm recover the starting cell with all its ionized neighbors marked as visited, it stops.

To implement this method, a recursive scheme could be used as well as linked lists. We chose the second option as it limits the use of large stacks of memory. Let us also mention that for boxes of 1024^3 , we have parallelized the identification on the large box by cutting it in 16 sub-boxes. We thus do the identification on this 16 sub-boxes in parallel to accelerate the calculation. We reassemble the entire box after and merge the IDs.

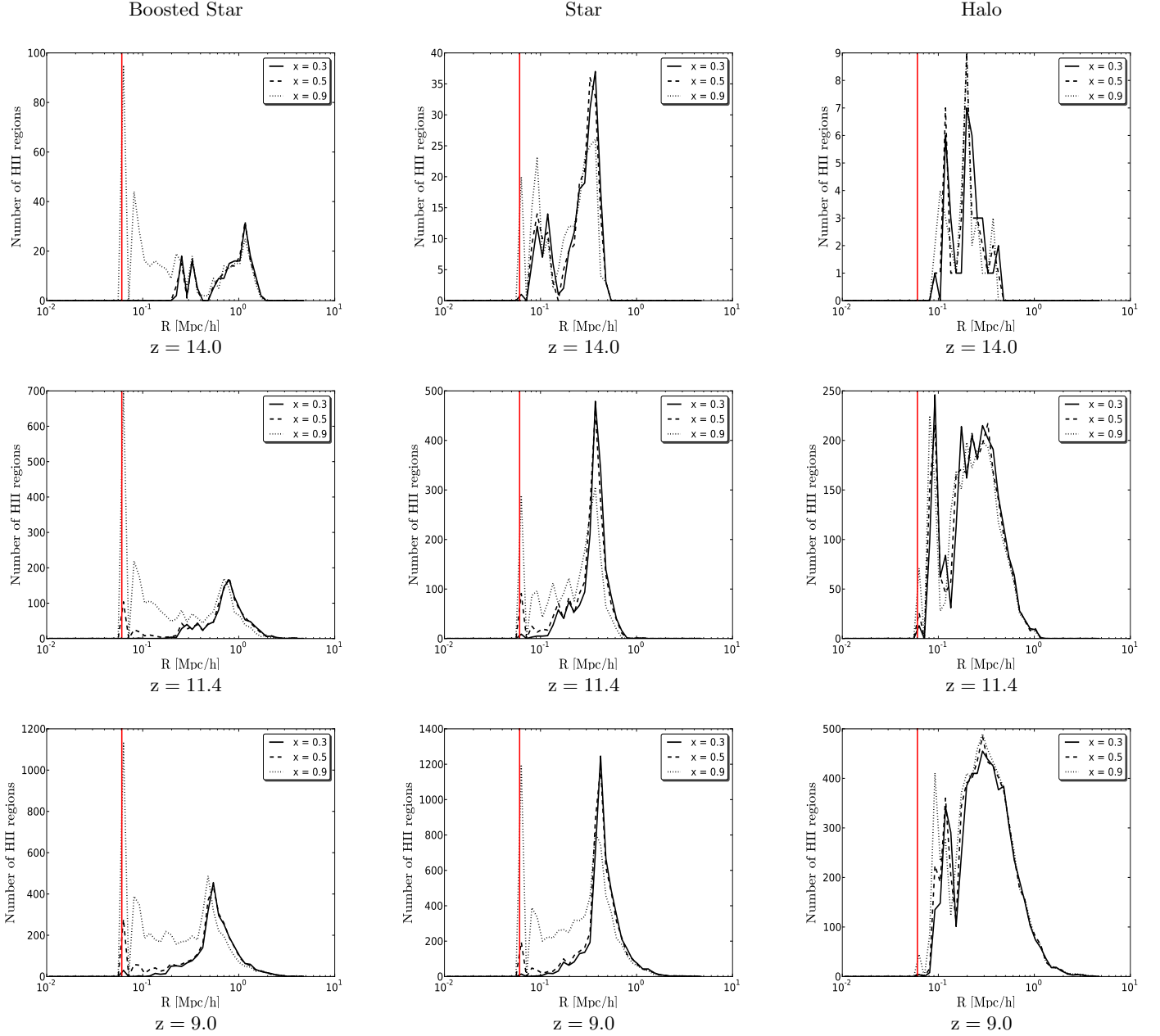


Fig. A.2. Representation of the radius distribution of all HII regions at three different redshifts for the three simulations for the 50 Mpc/h box. We compare the difference in the radius distribution according to the ionization threshold for the detection of the HII region with the FOF procedure. We represent the volume of one single cell with the vertical red line.

A.2. Effect of the neutral ionization threshold

The FOF algorithm assumes an ionization threshold in order to decide if a cell is ionized or not. As often used in the literature, we have chosen a value of $x \geq 0.5$ to consider a cell as ionized. In order to test the impact of the threshold's value for the identification of the HII regions we have also tried other values for the ionization fraction in the FOF procedure.

The figure A.2 represents the radius distribution of the HII regions for three different instants. The distributions are done for the three model of ionizing sources for the 50 Mpc/h box size. We compare the radius distributions according to three different ionizing thresholds of $x \geq 0.3$, $x \geq 0.5$ and $x \geq 0.9$ to assume that a cell is ionized. The

three distributions are very similar for all models and at each instant regardless of the chosen ionizing threshold. The most significant variation stands for small regions with radius below $\sim 2 \times 10^{-1}$ Mpc/h that are detected in greater number with $x \geq 0.9$. Meanwhile, the distributions with $x \geq 0.3$ and $x \geq 0.5$ are almost superimposed in every cases. Additionally, we used the merger tree properties to plot the same distributions in figure A.3 but dissociating the contributions of each type of regions. Thus new regions are in blue, expanding regions in red, regions resulting from mergers in green and the regions that will recombine in yellow. This time, we have just represented the distribution for both $x \geq 0.5$ and $x \geq 0.9$ ionization threshold, that previously exhibited the greater difference. We see that globally

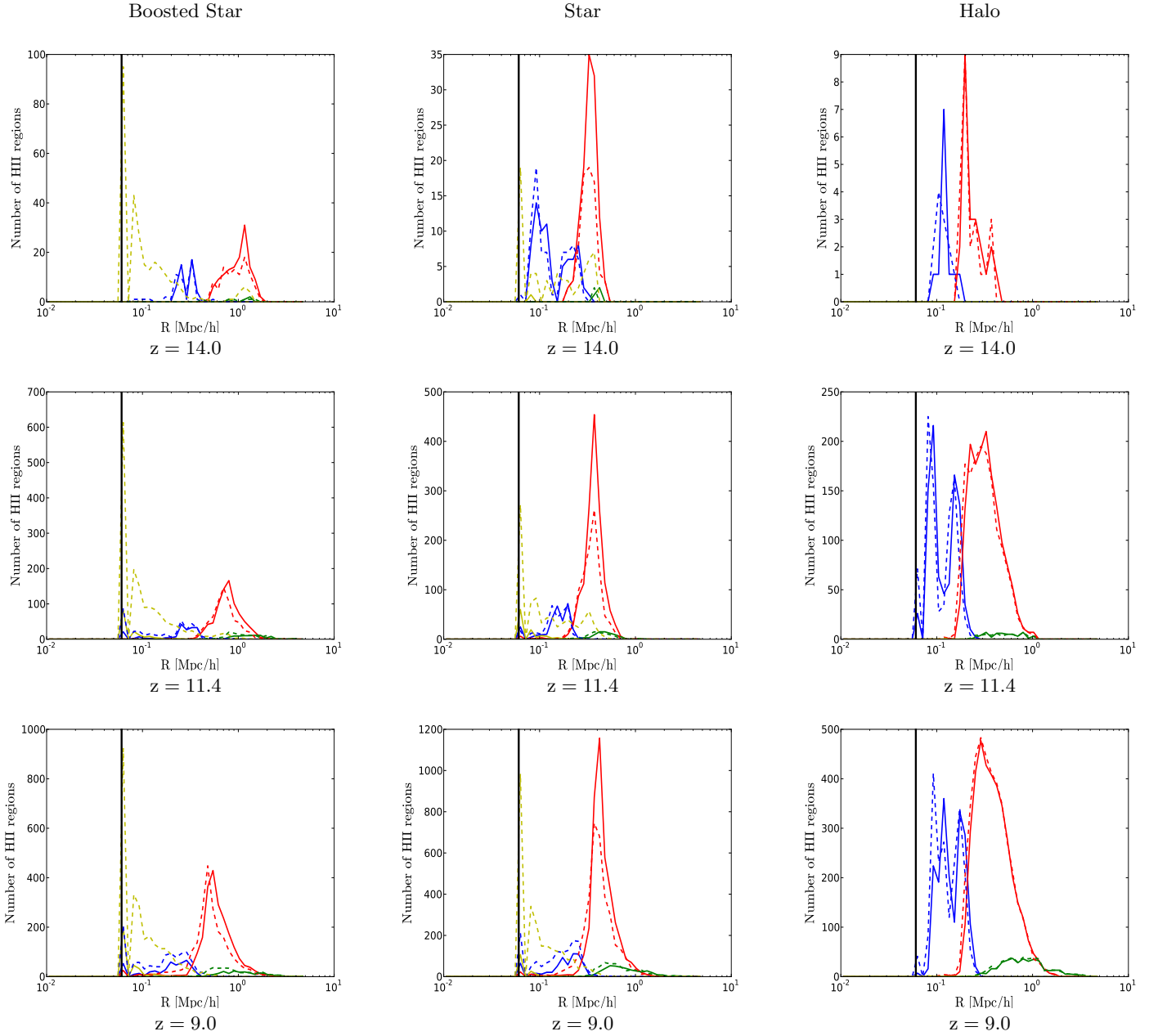


Fig. A.3. Radius distribution of all HII regions at three different redshifts for the three simulations for the 50 Mpc/h box. This time, we dissociate the distribution in the different counterpart of the type of HII region considered. We compare the difference in the radius distribution according to both ionization threshold of $x \geq 0.5$ and $x \geq 0.9$ for the detection of the HII region with the FOF procedure. The color codes are as follows: Blue: the new regions, Red: the expanding regions, Green: the regions resulting from merger and Yellow: the regions that will recombine. In addition we represent the volume of one single cell with the vertical black line.

that the families remain unchanged and therefore that the merger tree properties are conserved even when varying the ionization threshold. The only difference being that with $x \geq 0.9$ the FOF procedure tends to detect more small recombining regions than with $x \geq 0.5$ in the boosted star and star models.

Therefore the only remarkable effects by varying the threshold is for high threshold values within recombining regions, that represent a tiny number and volume fraction of the HII regions network. It does not come as a surprise though, since recombination occur in already ionized re-

gions and any fluctuations within, combined with a high detection threshold lead to a subdivision of regions in smaller ones. One might even consider that such effect should be avoided since it increases branches in the merging tree with regions that may be short lived or unstable. As a conclusion, we can thus consider that the value of $x \geq 0.5$ used in the paper for the identification of the HII regions is a good compromise, in addition of being the one commonly used in the literature.

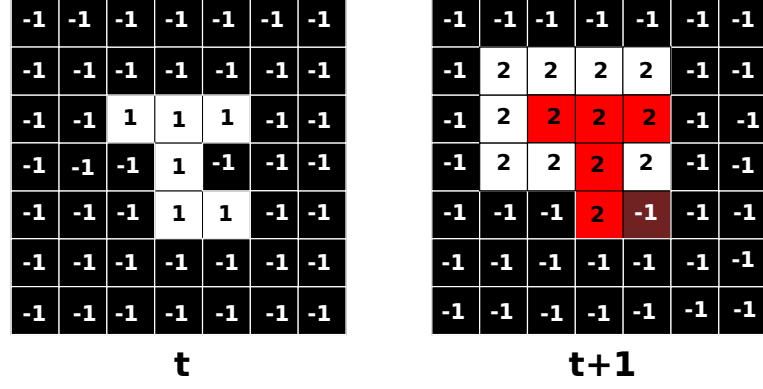


Fig. B.1. Merger tree algorithm. All neutral cells are black with an identification number of -1. All ionized cells are white with an identification number. At time t , we have the ionized region identified with an identification number of 1. We look forward at time $t+1$ where cells of this ionized region are located (shown in red). Here ID 1 at time t is linked to ID 2 at time $t+1$.

Appendix B: Merger tree algorithm

The implementation of the merger tree algorithm is performed as follow (see also Figure B.1):

1. We look at an instant t of the simulation where are located the cells of a particular ionized region. They all share the same ID.
2. Then, we extract the same cells at time $t+1$. These cells may have different IDs.
3. The most common ID at time $t+1$ is kept and is linked to the ID investigated at t .

This scheme is repeated for all HII regions between the snapshot t and $t+1$. We finally reproduce this process between each snapshots.